USE OF THERMAL ANALYSIS FOR EVALUATION OF INOCULATION EFFICIENCY
IN NODULAR CAST IRON

ANTÓNIO JORGE FERREIRA PIRES
MASTER'S THESIS
ENGINEERING FACULTY OF THE UNIVERSITY OF PORTO

SUPERVISOR:

PROFESSOR DOCTOR CARLOS SILVA RIBEIRO

DOCTOR LEANDER MICHELS

U.PORTO

FEUP FACULDADE DE ENGENHARIA
UNIVERSIDADE DO PORTO

Candidato	António Jorge Ferreira Pires		*Código*	201504416
Título	Use of Thermal Analysis for Evaluation Of Inoculation Efficiency In Nodular Cast Iron			

Júri	*Presidente*	Luís Filipe Malheiros de Freitas Ferreira	DEMM - FEUP
	Arguente	Daniel Santos	Siemens - Gamesa
	Orientador	Carlos Alberto Silva Ribeiro	DEMM-FEUP

DATA	*28 de julho de 2020*
HORA	*14h00*

"A utopia está lá no horizonte. Me aproximo dois passos, ela se afasta dois passos. Caminho dez passos e o horizonte corre dez passos. Por mais que eu caminhe, jamais alcançarei. Para que serve a utopia? Serve para isso: para que eu não deixe de caminhar."

Eduardo Galeano

PROLOGUE

This work comes after a cooperation agreement between ELKEM – Norwegian ferrosilicon inoculant and spheroidization manufacturer acting worldwide, and Faculty of Engineering of University of Porto – Department of Metallurgy and Materials, as a final Master dissertation work of the Integrated Master on Metallurgy and Materials aiming the validation of thermal analysis techniques as a swift tool to evaluate inoculation efficiency in ductile cast irons. Trials have been made in Kristiansand ELKEM laboratories in Norway, using regular and dual closed cartridges as well as step castings.

The first chapter addresses the bibliographic up-date of the subject of the nodular treatment procedure and the use of the thermal analysis technique.

The second chapter addresses the experimental procedure while in the third chapter, it was elaborated a critical evaluation of results of chemical characterization and cooling curves of the samples and the microstructure parameters, such as nodule count, size distribution, nodularity. In the end, it was made some conclusions of this work.

MOTIVATION AND OBJECTIVES

The motivation for the implementation of this work rose, not mainly, from the great opportunity and experience of doing an internship at ELKEM Technology in Kristiansand, but also for the interesting project which was proposed to me.

In cast iron, the presence of carbon and its segregation into graphitic layers affects the overall morphology and mechanical properties of the end-product, the casting itself.

Inoculation is a way of controlling the structure and properties of cast iron by minimizing undercooling and increasing the number of graphite particles - nodules (for nodular iron) during solidification.

With time, the effectiveness of inoculant decreases, being a problem to the production of SG (spheroidal graphite) iron cast therefore, the goal of this work is to validate how well and if thermal analysis could be used as a tool to follow the inoculation effectiveness and fading resistance of two inoculants [(Ca,Al)FeSi and (Ba)FeSi] during the solidification of nodular cast iron.

ABSTRACT

This Master's Thesis focuses on the analysis of the immediate efficiency and fading resistance of two inoculants in ductile cast iron melts, using thermal analysis technique. Three types of samples have been made: two thermal analysis cartridges - standard open cup, a closed dual cup and a step casting with section thicknesses of 20, 10, and 5 mm.

The inoculation efficiency was evaluated through the type of graphite in the microstructure, nodules density (per mm^2), nodularity, nodule size, and the existence of carbides or not, relating them with arrests and critical points, following the cooling and solidification of cartridge samples using thermal analysis.

For the base melt with hyper-eutectic chemical composition, the melt was inoculated with two distinctive inoculants: a (Ca, Al)-containing ferrosilicon, and a Ba-containing ferrosilicon. For both inoculated melts, the pouring ladles were kept at three different times before sampling and pouring into sand moulds/ cartridges: 1 minute - immediate inoculant behaviour, 10 minutes, and finally 20 minutes – fading resistance behaviour.

The results from the dual cups show that TEu_{Low} and TEu_{Up} decrease with time for the Ca-inoculated melts as a result of fading effect of the Ca-FeSi inoculant, while no decrease of TEu_{Low} and TEu_{Up} were observed for the Ba-inoculated melts which means that Ca-FeSi inoculant has greater immediate effectiveness and lower resistance to fading than the Ba-FeSi inoculant.

In the dual cup's microstructures, it was observed an increase in nodule count and nodularity with time, which was unexpected.

The results of the standard open cups showed a discrepancy with the solidification morphology of the cooling curves and the chemical composition of the melt, and therefore it was concluded that the open cup is not the best option when you want to anticipate in real-time, while solidification occurs, the type of microstructure resulting from solidification of the melt.

For the step castings, no correlation was possible to make since liquidus temperature of most of the cooling curves were not recorded and therefore no reliable results could be presented.

KEYWORDS

ACKNOWLEDGEMENT

AGRADECIMENTOS

Durante esta experiência única, eu tive o privilégio de estar em contacto com muitas pessoas, que, agora, lhes devo o meu profundo agradecimento e gratidão.

Primeiramente, estou bastante agradecido ao meu orientador Professor Dr. Carlos Silva Ribeiro por me confiar este projeto, por me guiar e me direcionar neste programa de estudos. Mas o mais importante foi por ter tido um enorme impacto na minha educação e por me despertar o interesse pela área de fundição.

Gostaria de agradecer ao meu outro orientador Dr. Leander Michels pela sua infinita dedicação e paciência, pelos conselhos e pelas preciosas colaborações em me guiar a editar o meu trabalho.

Tem sido uma grande honra para mim trabalhar com os meus supervisores a quem devo a gratidão por partilharem os seus conhecimentos excecionais e as suas experiências em fundição.

Para além disso, agradeço ao Dr. Eivind G.Hoel pelo seu suporte, pelo seu excelente profissionalismo e por ajudar a desenvolver o procedimento experimental. Também preciso de agradecer ao resto do departamento de I&D por me receber tão calorosamente durante a minha estadia na ELKEM e pelos saberes que me transmitiram.

Quero manifestar a minha gratidão aos meus amigos da universidade, especialmente à Inês Silva, Joana Freitas e ao João Dias, que me proporcionaram inúmeras memórias e intercâmbio de conhecimento durante esta etapa da minha caminhada às quais vou guardar com todo carinho.

Aos amigos mais próximos, Bruna Santos, David Conde, Mafalda Moutinho, Marcos Devesa e Marta Ribeiro que formam comigo um grupo que está sempre pronto para jantares, para partilhar grandes momentos e em todos os momentos.

Quero ainda expressar o meu profundo agradecimento aos meus pais e à minha irmã por me encorajarem continuamente ao longo de todos estes anos de estudo, por fazerem sempre tudo para me garantirem as condições necessárias para trabalhar e ser bem sucedido.

Gostaria de estender o meu agradecimento a toda a minha família e a três fantásticos amigos que considero muito, Eduarda Coelho, Manuel Pinto e José Manuel Pinheiro que, pessoalmente ou à distância, cuidaram de mim e ajudaram a manter-me motivado.

Finalmente, fico grato por todos aqueles que caminharam ao meu lado. Todos contribuíram para o meu crescimento intelectual e formação pessoal tornando-me aquilo que sou hoje.

Obrigado!

CONTENTS

LIST OF TABLES

LIST OF FIGURES

ABBREVIATIONS AND SYMBOLS

Al - Aluminium
Ba – Barium
C - Carbon
Ca – Calcium
CCA -Cooling Curve Analysis
CE – Carbon Equivalent
Ce- Cerium
DCI – Ductile Cast Iron
DNV GL® - International accredited registrar and classification society headquartered in Høvik, Norway
FeSi – Ferrosilicon
Mg - Magnesium
Mn – Manganese
MSI - Metal Stream Inoculation
O - Oxygen
P - Phosphorus
REE – Rare Earth Elements
S - Sulphur
SG – Spheroidal Graphite
Si – Silicon
Sr – Strontium
Ti - Titanium

1. PRELUDE

Ductile Cast Iron – DCI has been widely used since the last sixty years, or so, as cheap ductile cast iron, to substitute malleable iron and some cast steel castings, mainly in the automotive industry components. Nowadays is the second most cast alloy, after lamellar iron, and represents about 25% of the world cast production.

To produce DCI producers have to use suitable non-contaminated metallic materials and the process involves two treatments after melting techniques: so-called nodularization – the early name used since 1960 or graphite spheroidization – a more modern name, to introduce a melt scavenger such as magnesium, which desulfurizes and deoxidizes the melt, and inoculation to promote graphite precipitation, instead of carbide precipitation [1]. This late technique is a request and is very sensitive because there are different practices which involve the way inoculant is added – primary or late inoculation, the chemical composition – normally ferrosilicon with some proprietary active elements, grain size distribution and amount of late addition.

In the inoculation practice, one considers the immediate effect after inoculant dissolution and fading effect. There are inoculants which behave nicely as the immediate effect, such as standard FeSi inoculant with Ca and Al as active elements, and some more vigorous inoculants, which have Ba, Sr, Ce, O, S, Mn.

This work addresses the comparison of the standard FeSi (with Ca and Al as active elements) with Ba containing FeSi inoculant, comparing the immediate effectiveness, and fading resistance, using thermal analysis techniques, and validating with the metallographic standard characterizations.

2. LITERATURE REVIEW

2.1. Characterization of Ductile Cast Iron

Cast irons are classified by their microstructures, primarily by the form of the excess carbon. This excess carbon may be presented in the form of a compound, such as Fe_3C (iron carbide or cementite) being classified as White Cast Iron, or as graphite classified as Grey Cast Iron. Within the grey cast iron class, there is still a classification according to the shape of the graphite particles that are formed during solidification, being classified as:

- Lamellar Graphite Cast Iron;
- Ductile Cast Iron (also named Nodular Graphite Iron or Spheroidal Graphite Cast Iron);
- Compacted Graphite Cast Iron;
- Malleable Iron.

DCI is characterized by having carbon in the form of spheroidal graphite, distributed across the iron matrix (see **Figure 1**) [2, 3]. The matrix unalloyed of ductile iron can vary from fully ferritic to almost fully pearlitic, with a resulting increase in strength and hardness (see **Figure 2**) [4]. The nature of the matrix depends on the addition of alloying elements (such as Cu and Sn to increase the pearlite content), cooling rate (higher cooling rates increase the pearlite content) and graphite particle density (higher graphite particle density will increase the amount of ferrite) [2, 3].
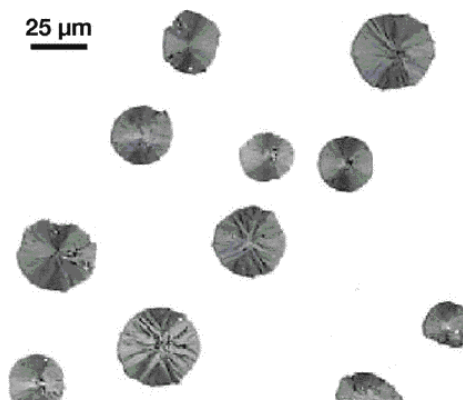
Figure 1.Typical microstructure of ductile cast iron, containing nodular graphite embedded in iron matrix. Not etched [5].
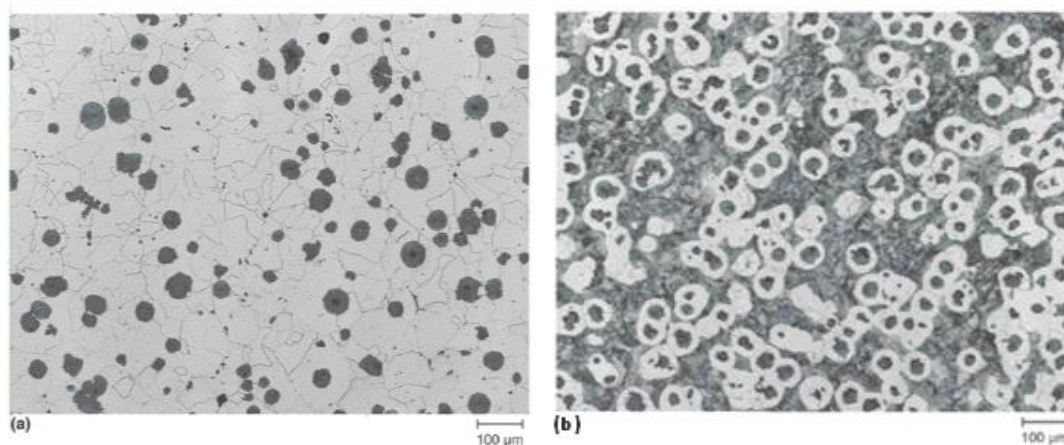
Figure 2. Typical DCI's graphite: (a) involved in fully ferritic matrix (b) involved in 40% ferritic and 60% pearlitic matrix. Both etched with 2% Nital [4].

Ductile irons are widely used due to their mechanical properties: good strength combined with good machinability and low production cost, with typical tensile strengths ranging from 380 to 900 MPa, a yield strength ranging from 200 to 600 MPa and elongations up to 22%. The matrix nature, the inclusions, the shrinkage porosity content and distribution, the shape and nodule count of the graphite particles have a strong impact on the mechanical behaviour of the material [3]. Nodularity exerts a strong influence on the yield and tensile strengths of ductile iron. When nodularity is reduced, the yield strength and tensile strength decreases [6].

Nodule count also influences the mechanical properties of ductile iron, although not as strongly and directly as graphite shape. Generally, high nodule count indicates good metallurgical quality, but an excess of this nodule count may result in a degradation of properties [6]. The market for ductile iron applications is led by automotive and nautical industries, transmission equipment, industrial equipment and machinery, energy generators, among others due to the economic advantages and reliability of the material.

2.2.   Metallurgy of Ductile Cast Irons

2.2.1. Chemical Composition and Process

The manufacturing of high-quality ductile iron begins with the careful selection of raw materials that will give a relatively pure cast iron, free of the undesirable residual elements such as phosphorus, chromium, or cobalt. The base iron raw composition to produce nodular cast iron is typically composed by steel scrap, special-quality pig-iron supplied for nodular iron production (S<0.03%, P<0.08%, Mn<0.5% or lower depending on the pig-iron grade) and nodular cast iron returns.

The essential elements in the composition of nodular cast iron are carbon, silicon, sulphur, and magnesium, while the other elements such as manganese, phosphorus and copper are pernicious and must be held at specified levels. **Table 1** shows the typical final chemical composition of ductile cast iron.

Table 1. Typical final chemical composition of the final SG iron in the casting [1, 7, 8]

Elements	%C	%Si	%Mn	%S	%Mg
	3.60-3.80	1.80-2.80	0.10-0.25	0.008-0.015	0.03-0.055

Magnesium, cerium and other elements must be controlled to attain the desired graphite shape and offset the deleterious effects of elements such as antimony, lead, titanium, tellurium, bismuth, and zirconium. These elements interfere with the spheroidization process and must be either eliminated or restricted to very low concentrations [1, 8].

Due to the requirement of low sulphur content for the base iron melt, usually it is subjected to a desulphurization step that can use magnesium (pure Mg or Mg-FeSi alloys with high Mg content) that it is added as lumps or as wire [7]. Nevertheless, the sulphur content in the final base iron melt should not be below 0.008% [8].

2.2.2. Influence of Si and Other Elements on Ductile Iron

Many elements found in commercial cast irons influence the eutectic composition. They either lower or raise the carbon content of the eutectic composition. The most important element influencing the eutectic carbon content is silicon. Silicon lowers the solubility of carbon in the melt, which lowers carbon content and increase the eutectic

reaction (moves to the left), causing also a reduction of the austenite field area (γ) on the Fe-C phase diagram, as illustrated in **Figure 3** [9].
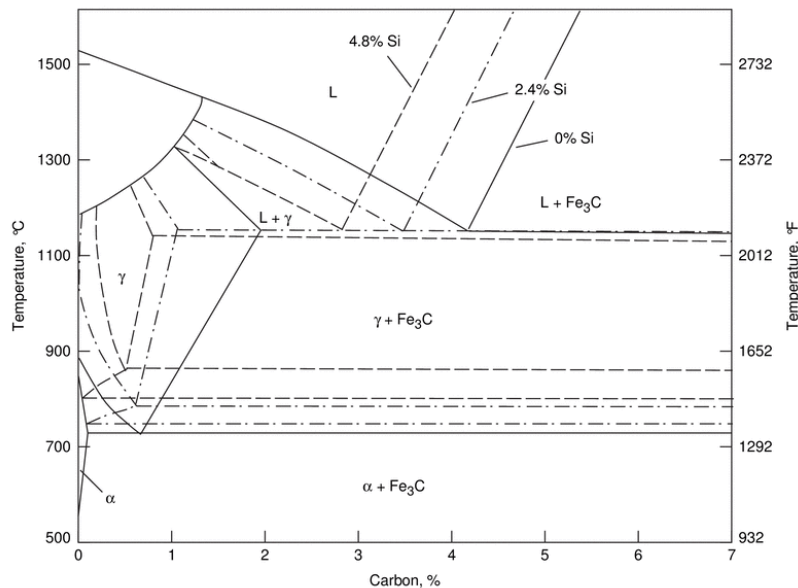
Figure 3. Effect of silicon content on iron-carbon phase diagram [10].

Silicon is a graphitization element, increasing the carbon activity in the melt, promoting the stable solidification of carbon into graphite, instead of the metastable solidification [3], and it is often described as a substitutional element for carbon in a "carbon equivalent" relationship. The most used relationship is:

$$Carbon\ equivalent\ (CE) = \%C + \frac{\%Si + \%P}{3} \qquad (\textbf{\textit{Eq}.1})$$

There are other elements in the melt that change a lot the equilibrium diagram Fe-C (see **Figure 4**). These changes make it difficult to predict, through the diagram, the final microstructure of the ferrous alloys, especially when it comes to eutectic alloys.
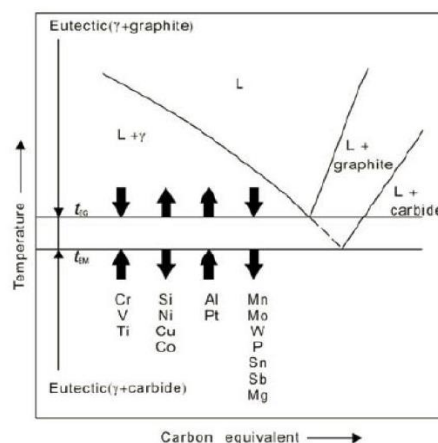
Figure 4. Effect of alloying elements on the stable and metastable temperatures in the Fe-C diagram [11].

2.2.3. Nodularization or Graphite Spheroidizing Treatment of SG Iron

The nodularization process consists on the addition of spheroidizers elements to reduce the oxygen and sulphur contents and achieve a desirable content of these elements that allow the growth of graphite with the spheroidal shape, to obtain ductile cast iron [3].

According to Ellingham's diagram (see **Figure 5**), the addition of Mg or other spheroidizers elements (Mg, Yttrium (Y), Ce, Ca and Lanthanum (La)), promotes the desulfurization and deoxygenation of the liquid metal, since Gibbs energy for the formation of magnesium oxide (MgO) or magnesium sulphide (MgS) is very negative so the formation of these sulphides and oxides occurs spontaneously, so the Mg has a strong affinity with sulphur and oxygen.
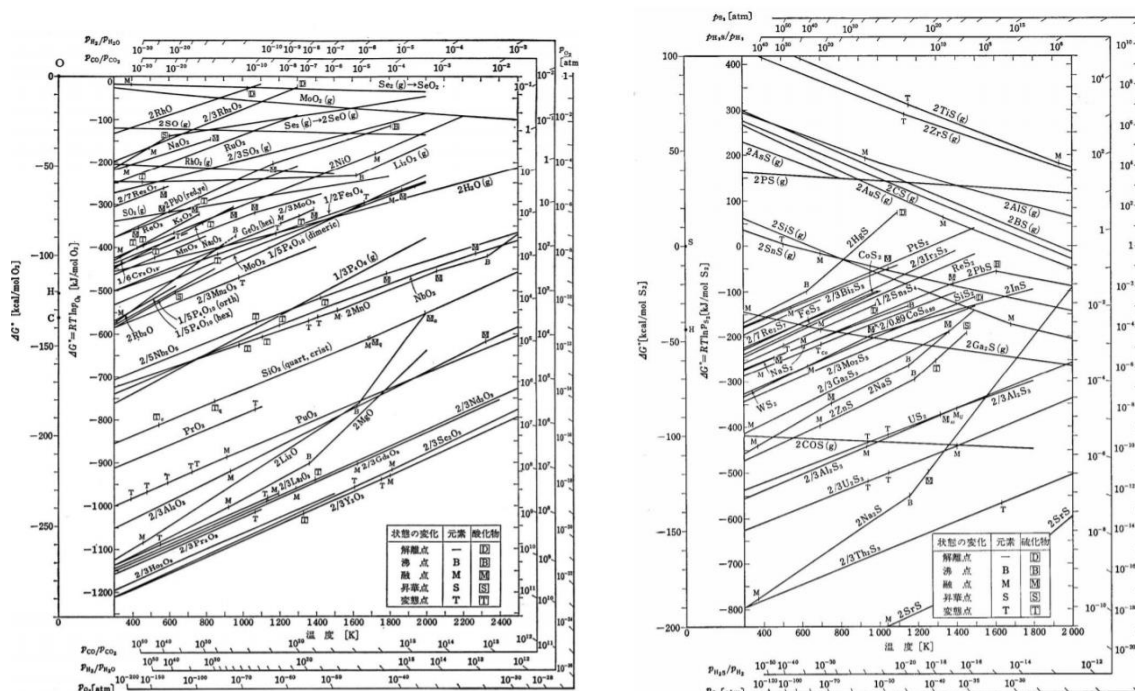
Figure 5. Ellingham's diagrams for Oxides and Sulphides, respectively [12].

Industry favours a nodularizer based on Mg-FeSi alloys, which contain commonly between 3 and 20% magnesium [13].

In the spheroidization treatment, traditional treatment methods are used, such as the Sandwich method, the Tundish-cover method or flux wire. In the Tundish-cover method (**Figure 6**), the Mg-FeSi alloy is placed in a compartment at the bottom of the ladle before the liquid metal is poured. Since magnesium isn't an easy element to add to a cast iron melt, due to lower density of Mg compared to iron, the limited solubility of Mg in cast iron and the boiling point being lower than the freezing point of cast iron, the Tundish-cover ladle, as it is shown in **Figure 6**, has a cover for the ladle to improve Mg recovery to reduce glare, fume and contain the strong reaction [1, 3].
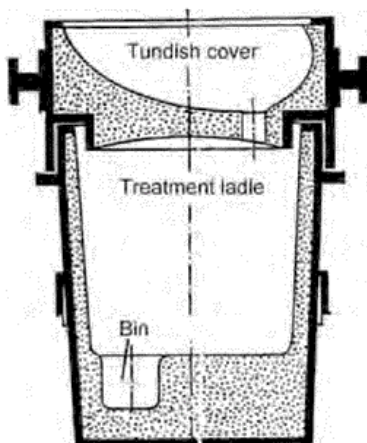
Figure 6. Treatment ladle for the Tundish cover process [14].

It is common to observe deterioration in the nodule shape of graphite, often referred to as fading of nodularity. Mg tends to be lost with time after their addition- also known as fading, from cast iron melts, due to two factors: (1) vaporization because partial pressure is well above 1 atm, at cast iron processing temperatures and (2) desulphurisation and deoxygenation. When residual magnesium becomes insufficient, poor nodules shape will occur [15].

2.2.4. Inoculation Treatment of SG Iron

After spheroidization treatment, sulphur and oxygen contents in the liquid iron are significantly reduced, and the Mg dissolved in the melt increases eutectic undercooling which, without inoculation, will promote carbide precipitation. However, the iron after spheroidization, but without inoculation, has fewer graphite nuclei, strong chilling tendency and poor mechanical property and therefore, after spheroidization, the iron must be inoculated [13].
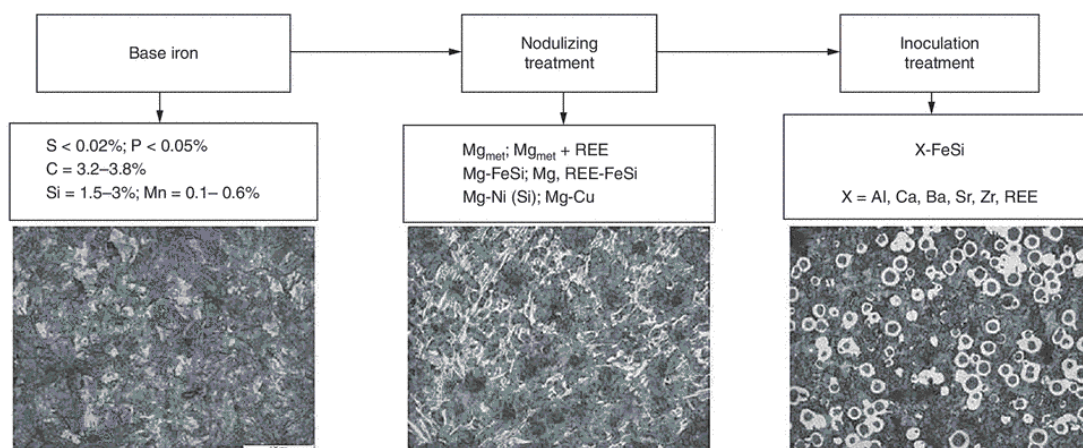
Figure 7. Ductile iron production flow chart and typical microstructures. REE, rare earth elements [1].

Figure 7 shows the beneficial effects of inoculation on nodular cast irons. An untreated base iron, as a reference, appears to be very sensitive to forming carbides. With nodularization treatment, the cast iron will be more likely to form carbides, so it is with inoculation treatment that carbide free microstructure will be promoted. Instead of that, there is the presence of very spheroidal graphite surrounded by a ferrite and pearlite matrix [1].

Inoculation is applied to the molten iron immediately prior to pouring melt to the mould, with direct effects on the primary structure since graphite is a non-metallic phase, which must nucleate and grow, in cast iron melt.

Before inoculation, the thermodynamic driving force for graphite precipitation is low. Graphite nucleation is difficult and delayed and requires very high undercooling, with the danger of carbides' precipitation. For graphite precipitation to occur, there is a need to promote nucleation of the graphite and produce a high chemical driving force. The former is produced by inoculation of the molten metal and the latter produced by increasing the carbon activity [9].

Inoculation aims to ensure that sufficient nuclei sites are available in the melt for the crystallization of graphite at the beginning of eutectic solidification, and prevent the formation of iron carbides [1].

Inoculant alloys usually have a so-called portable system FeSi alloys, easily soluble in cast iron melts, and one or more active X elements, where X is calcium, barium, strontium, cerium, which are established inoculating active elements. The nucleating elements, when added to the melt, combine to form complex oxides or sulphides that act as active surfaces for the nucleation and subsequent growth of graphite [1, 16].

The inoculation treatment can be performed at different stages of the production process, although the addition of inoculants should be carried out as late as possible, shortly before or during pouring to the mould cavity [3, 17]. Depending on the nuclei effectiveness and cooling conditions, inoculation can take place: (1) during tapping the melt from the furnace while filling the ladle, normally after the Mg-alloys addition, also known as a ladle or primary inoculation, (2) in the pouring stream (metal stream inoculation – known in the industry as MSI) or (3) in the mould (mould inoculation – the most effective of them all) [3, 17].

The type of inoculant (depending on the chemical composition) and this moment of addition depends on the process used and of the castings produced [3, 7].

The size distribution of the inoculant depends on the holding time between inoculation treatment and pouring. In the ladle inoculation, coarser inoculant is used for longer holding times, usually between 5 and 10 mm. In the late stream inoculation treatment, the inoculant particles must have a calibrated size between 0.5 and 2 mm [3, 7].

The inoculation treatment establishes a favourable nucleation state influencing both the graphite precipitation (number, size, shape) as well as promoting the grey solidification and preventing of a ledeburite chill [1, 17].

The addition of inoculant promotes more efficient nucleation of graphite, increasing nodules density, graphite nodularity and a decrease into nodules size [3].

Effective inoculation leads to uniform mechanical properties in different thicknesses sections, especially to a restriction of the hardness scatter, becoming less dependent on the cooling rate [1, 17]

It is revealed that the inoculation treatment is very important for the treatment of SG cast iron. However, carbide formation can still occur after an effective inoculation due to the fading characteristic of the inoculation treatment.

2.2.5. Fading of Inoculation

As holding time, after inoculant addition, increases, the effect of inoculation – number and nodularity, of graphite particles - are gradually lost; this is called fading of inoculation. The working time of inoculation for SG iron is about 12 – 15 min. Inoculation's fade is worsened with increasing holding time, with increasing treatment temperature, strong stirring, increasing white iron – steel scrap contents, in the melting charge, too fine inoculant particle size and high sulphur and oxygen contents in base iron melt. The fundamental reason for inoculation's fade is the reduction of heterogeneous nuclei in the molten metal iron [18].

With conventional inoculation, the effects of the inoculant begin to fade instantaneously, and it has been shown that the number of sites available for nucleation deteriorates. **Figure 8** shows the fading effect, after inoculant addition but before pouring, on the number of eutectic grains (cells) as well as the efficiency of various inoculants on Lamellar Graphite Cast Iron [18].
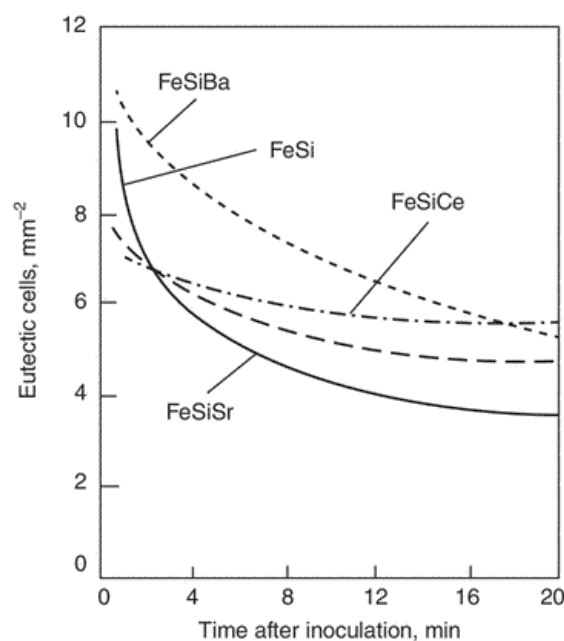
Figure 8. Fading of inoculation [18].

Different inoculants have different reaction and dissolution times, depending on the nature of the active elements they have and initial S content in the melt. For example, according to **Figure 8,** the inoculant containing strontium has stronger immediate

effectiveness, however inoculant containing strontium has a high fading effect, so this inoculant is better for late inoculations.

During melting and subsequent spheroidizing and inoculation treatment, many non-metallic inclusions are produced in iron melt; these primary inclusions are very small in size and can grow with time [16].

According to Skaland, inoculation's fading is explained by the Ostwald ripening effects where there is the coalescing of the nuclei population which causes the total number of potential nucleation sites to be reduced [16]

2.3. *Conditions for Graphite Formation in Ductile Cast Iron*

Graphite formation in ductile cast iron is divided into two stages: nucleation and growth; nucleation is the first process of graphite formation which later may grow as lamellar, vermicular or spheroid graphite [13].

2.3.1. Nucleation of Spheroidal Graphite

Homogeneous nucleation of graphite is very unlikely to happen in cast iron because there are impurities in the melt, that act like nuclei sites and therefore, the nucleation barrier, for heterogeneous nucleation, is much lower than for homogeneous nucleation [19].

A wide variety of impurities have been suggested as nuclei for SG cast iron, such as oxides, silicates, sulphides, carbides, nitrides and other intermetallic compounds [13, 16, 20].

Oxides have been identified in the nuclei of SG by a larger number of investigators, including Heine and Loper, Poyet and Ponchon [Magnesium oxide (MgO), Silicon dioxide (SiO$_2$)], Jacobs and Skaland (Mg, Al, Si,Ti oxides) [20].

The classic model for heterogeneous nucleation is shown schematically in **Figure 9**. Here the graphite phase (G) grows from the nucleant (N), and the geometry of the graphite phase is a segment of a sphere of radius r and contact angle Θ [16].
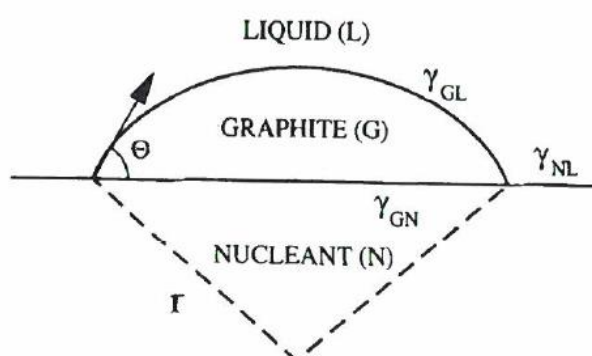
Figure 9. Schematic representation of heterogeneous nucleation [2].

To have good nucleation, graphite must wet (as much as possible) completely the substrate which means that Θ=0 and there is no energy barrier to nucleation. The value of free energy barrier (ΔG*) depends, in turn, on the crystallographic disregistry between the substrate and the nucleated solid or, in other words, depends on the difference between the lattice parameter of the substrate and the nucleated solid for a low-index plane. In practice, the undercooling increases with increasing values of the planar lattice disregistry (δ), as it shows in **Figure 10** [16, 21].
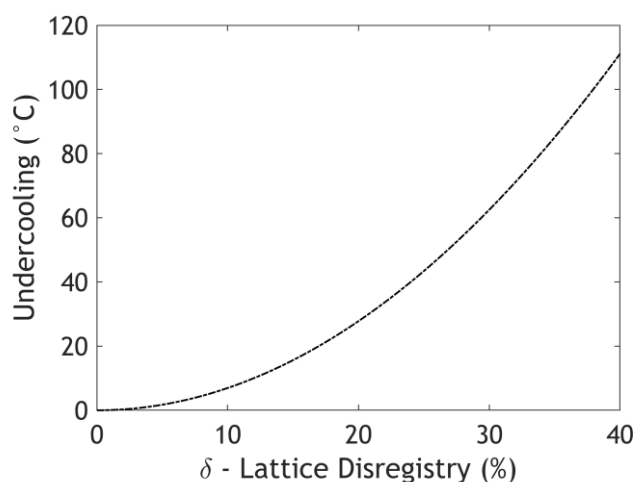
Figure 10. Characteristic undercooling vs planar lattice disregistry [16, 21].

Since the inoculant promotes heterogeneous nucleation with the decrease of undercooling, the planar lattice disregistry between the inoculant promoted phase and the graphite is low. Hence, they have coherent/semi-coherent interfaces.

According to Jacobs [1], graphite nodules nucleate heterogeneously on particles, which were formed in the melt and exhibited a duplex sulphide/oxide structure (**Figure 11 (b)**). These nucleating particles consist of a central seed surrounded by an outer shell of different crystal structure [1].

For Ca-FeSi and Sr-FeSi inoculated, Mg-FeSi treated iron, it was found on the "central seed" (Ca,Mg)S or (Sr,Ca,Mg)S compounds, respectively. Nevertheless, the mismatch between (Ca,Mg)S, (Sr,Ca,Mg)S and graphite is relatively bigger: a single sulphide is very difficult to directly become an effective substrate for graphite precipitation [1, 16, 20].

So, Jacobs proposed that graphite nuclei particles are surrounded by an oxide shell: an (Mg,Al,Si,Ti)oxide that has an orthorhombic or hexagonal structure. It appears that magnesium, calcium, and strontium play two important roles in ductile iron nucleation: (1) - to combine with and remove the free sulphur from the melt, and (2) - to promote sulphide particles formation, with both roles being important and necessary to graphite nucleation [1, 20].

However, Skaland proposed a mechanism for inoculation, where graphite can precipitate effectively. When the melt is inoculated with ferrosilicon containing active elements such as Ca, Ba, Sr and Al, these will create hexagonal silicates on existing

inclusions, making them more favourable sites for subsequent graphite nucleation (**Figure 11 (c)**) [1, 20].
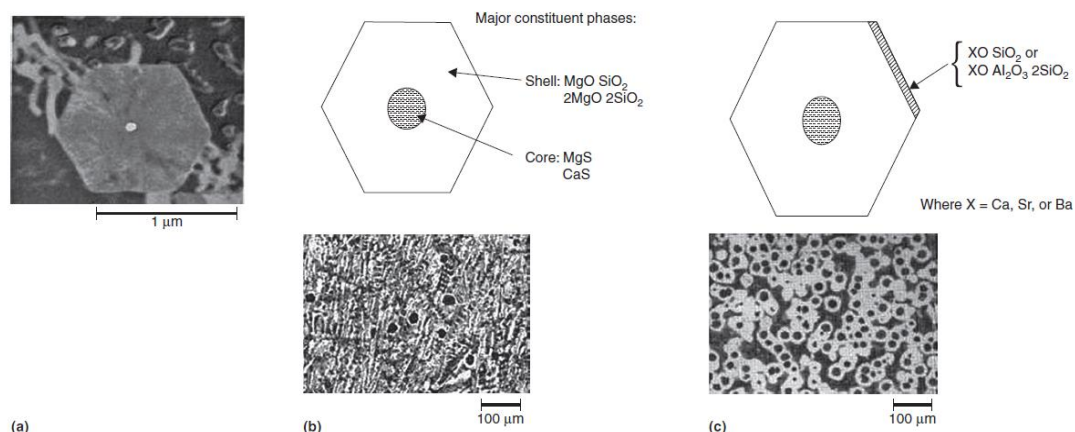
Figure 11. a) Duplex structure (sulfide/oxide) in MgFeSi treated iron. b) After Mg-FeSi treatment. c) After inoculation [1].

The potent desulfurizing elements—magnesium, calcium, and rare earth elements—are the first stage reactions, while silicon, aluminium, calcium, strontium, and barium—are associated to a second-stage reactions resulting in the formation of silicates [1].

2.3.2. Growth of Spheroidal Graphite

After nucleation, graphite starts to precipitate on the substrate to grow. The final graphite shape formed is dependent on the growth method influenced by processing conditions.

Figure 12 a) and Figure 12 b) shows a proposal to the crystallographic structure of the lamellar and spheroidal graphite, respectively.

A presence of surface-active impurities (S, O, Lead (Pb), Ti) tends to be adsorbed at the graphite interface reducing the prism plane $(10\bar{1}0)$ interfacial energy with the melt to a value below that of the basal plane (0001) therefore, the growth is predominant in the a-direction with the formation of lamellar (plate) graphite. When reactive impurities (Mg, Ce, or La) are added to the melt, they "remove" or capture in more stable phases the surface-active elements, and the preferred growth direction becomes the c-direction [13, 16, 20].

The growth in the c-direction occurs from the step of screw dislocations intersecting the interface and becomes a spiral during growth (**Figure 12 c)**).
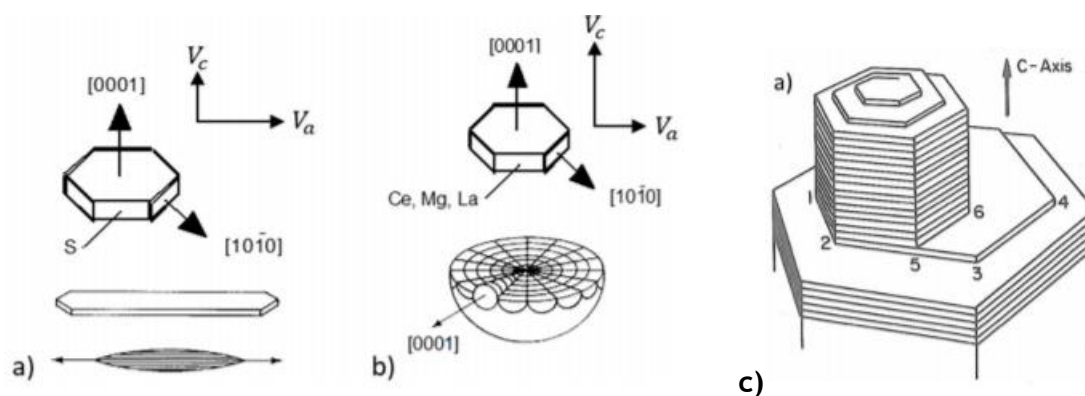
Figure 12. Change in the growth velocity of graphite due to adsorption of impurity atoms: a) Pure environment; b) environment contaminated with reactive impurities (Mg, Ce, La); c) Spiral growth by screw dislocation [20].

2.3.3. Effect of Solidification Rate on the Microstructure of Cast Iron

Nodular cast iron is sensitive to its section and has a significant impact in the microstructure development. Section thickness mainly affects solidification and cooling rates, but it can also affect the magnesium fading (transition from round nodules to flake) if it had extended solidification times. These three factors influence nodule count, presence of carbides and the amount of ferrite and pearlite in the final microstructure [2].

Faster solidification rates, which are associated with thin sections, promote carbide in eutectic reaction and pearlite formation in eutectoid reaction, whereas slower solidification rates favour graphite and ferrite formation. Alloying elements, such as cooper (Cu), Tin (Sn), Manganese (Mn), chromium (Cr), molybdenum (Mo) and vanadium (V), will increase the fraction of pearlite [2].

Faster cooling rates promotes nucleation of graphite – giving rise to an increase of the number of graphite embryos which eventually became graphite nucleus. For the formation of graphite nucleus, two energies involved must be considered:

- change in bulk free energy, ΔGv, as the liquid transforms into solid;
- the energy contained in the surface of the particle (γ which is always positive) [10, 11].

The total energy change for a spherical nucleus will be the sum of the bulk and surface terms:

$$\Delta G_T = (\Delta G_v \cdot \frac{4}{3}\pi r^3) + 4\pi r^2 \cdot \gamma \qquad (\boldsymbol{Eq.\,2})$$

Where r is the radius of the particle and γ is the solid-liquid surface energy.

In heterogeneous nucleation of graphite, the inclusion presented in the melt provides nucleation sites for the graphite to form from the liquid phase, which decreases the

surface energy and reduces the critical radius [11]. **Figure 13** suggests the total free energy change as a function of the critical nucleus size, r*.
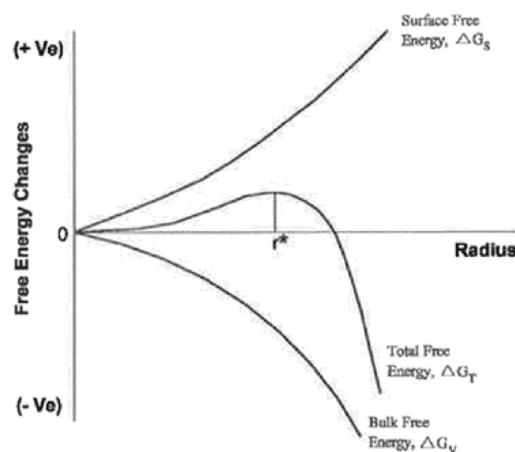
Figure 13. Free energy changes involved in the formation of a particle of radius r are plotted versus particles size [22].

ΔG_T is positive over a range of small particle sizes, and then rapidly becomes negative as the particle size increases. There is a critical radius (r*) which correspond to the maximum on the curve. Particles of a size smaller than r* will not survive in the melt, but larger particles than r* are able to grow [22].

Equation 2 can be rewritten in respect to r*, and setting the new equation equal to zero, yields the following equation for r*:

$$r^* = -\frac{2\gamma}{\Delta G_v} \qquad\qquad (Eq.\,3)$$

According to **Equation 3**, increasing the cooling rate will promote higher undercooling and the ΔG_v will decrease; therefore, the critical radius also decreases, which will increase the number of active graphite embryos in the melt (**Figure 14**) [23].
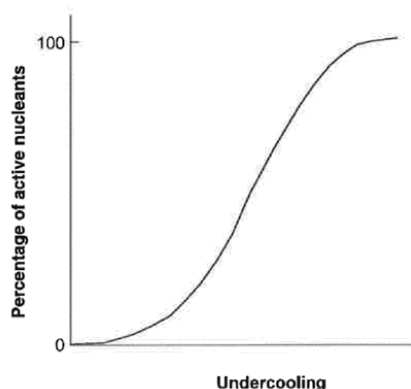
Figure 14. A hypothetical spectrum of the number of nucleus that become active as a function with undercooling [10].

Because of higher cooling rates, the density of nodules will increase, nodules size will decrease, and the apparent nodularity is improved when the size of the nodules decreases.

2.4.   Introduction of the Use of Thermal Analysis

Cooling curve analysis (CCA) is a method of measurement for thermo-physical characteristics of samples and is widely used for practical problem's solution.

The thermal analysis is based on the recording, mathematical manipulation and interpretation of cooling and solidification curves in real-time, as cooling and solidification of samples occurs, using thermocouples and simultaneous mathematical treatment on a portable computer, to identify the solidification phenomena of a sample [3].

Thermal analysis technique is widely used in foundry industries to control the solidification of cast irons and aluminum alloys, as well as the inoculation and nodularization process, during the treatment stage of melt [3].

2.4.1. Applicability of Thermal Analysis Technique

Thermal analysis is associated with the recording of a cooling curve from a sample which is cast in moulds – named thermal analysis cartridges, with a thermocouple inserted in its geometric center.

The thermocouple is connected to an A/D converter allowing the monitoring of the temperature variation with time, as solidification occurs [3, 24] and, with a suitable PC app, identify with accuracy all the arrests and inflections related to the solidification phenomena.

During the cooling of a melt, without any melt property change, the heat released must be equal to the evolution of the sensible heat of the sample, resulting into an exponentially decreasing curve, without inflections or arrests.

The cooling curve is featured by a temperature decrease over time, with the given slope $(\frac{dT}{dt})$. However, during solidification the transition from liquid to solid involves the release of latent heat of solidification (ΔH) [3, 24].

The released heat can be written as **Equation 4**, where V is the sample's volume, ρ is the density of the melt and C_p is the heat capacity and $(\frac{df}{dT})$ is the volume fraction of solid formed at a varying temperature [3, 24].

$$\frac{dQ}{dt} = V \times \rho \times C_p \times \rho\Delta H \frac{df}{dT} \times \frac{dT}{dt} \qquad\qquad (\boldsymbol{Eq.\,4})$$

According to **Equation 4**, the slope variation of the cooling curve and the occurrence of a plateau/arrest corresponds to the occurrence of physical or metallographic transformations.

In certain circumstances, the amount of heat released for the phase transformation might not be enough to produce a plateau in the cooling curve, just a change in the cooling rate with a slope variation.

2.4.2. Interpretation of Cooling Curves for Thermal Analysis

The analysis and interpretation are done by observing the critical points of inflection of the cooling curves, making it possible to correlate the microstructures of the alloys.

Sometimes it is difficult to identify the critical points of inflection of the cooling curves. Hence, it is common practice for thermal analysis cooling curves to be complemented by the first derivative and the second derivative of the curve, to increase the accuracy of the identification of the critical points [3].

All the critical points in the cooling curve are identified by a maximum and a minimum in the curve of the 1st (dT/dt) and 2nd (d^2T/dt^2) derivative as can be seen in **Figure 15**.
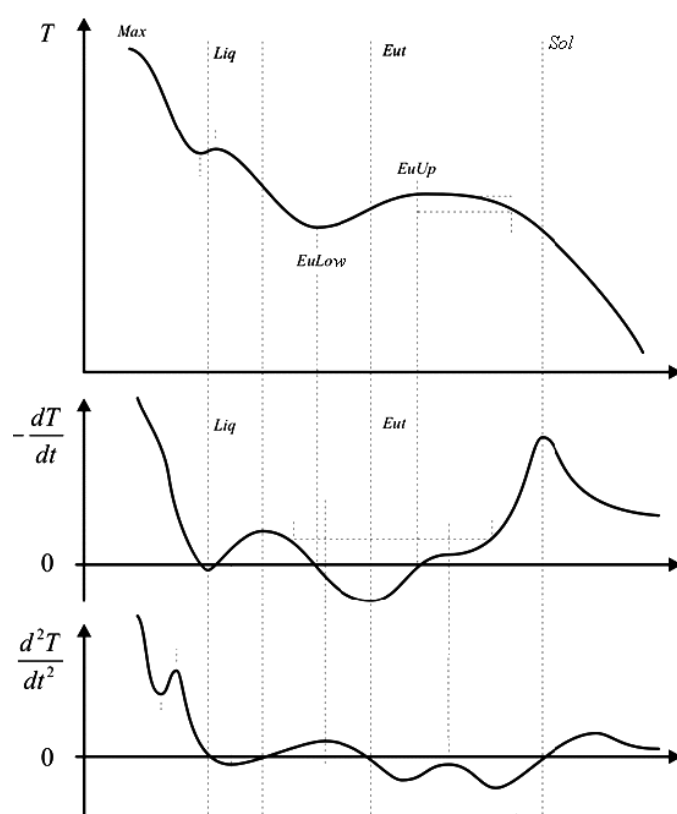
*Figure 15. Illustration of the temperature/time curve, the **inverse** of the 1st derivative and 2nd derivative [3].*

A thermal analysis curve example is shown in **Figure 16** where its main inflection points are identified. On the solidification of hypoeutectic alloy, it is expected a first plateau, or inflection in the cooling curve, because of primary austenite precipitation. After that phenomena, the slope of the cooling curve shall be small. A second plateau occurs during the eutectic reaction.

Both reactions are easily identified by the inflection they cause in the cooling curve during their occurrence [3, 24].
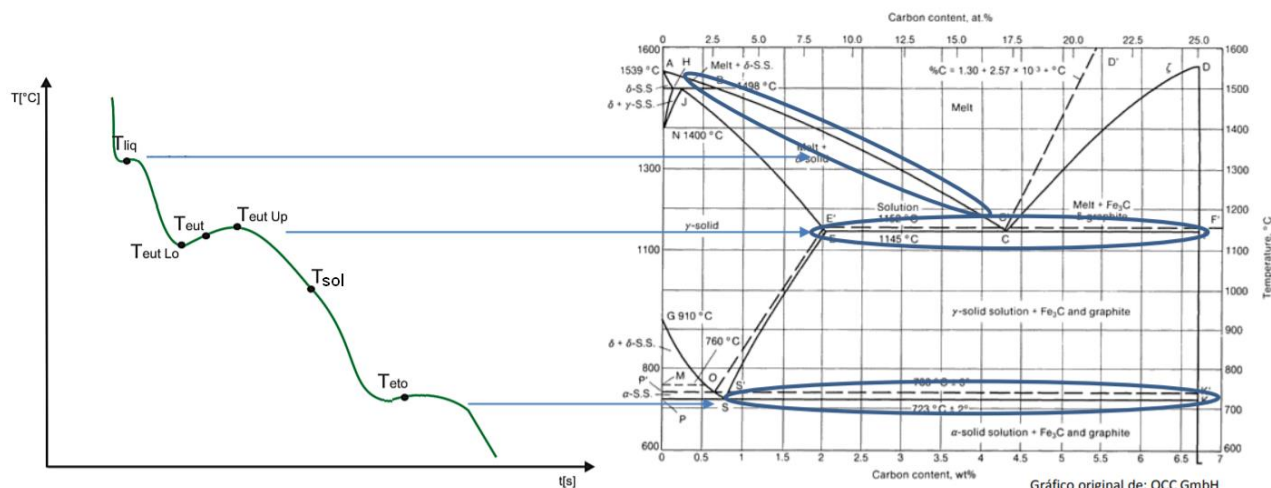
Figure 16. Identification of the main critical points in the cooling curve with the support of the diagram Fe-C [24].

On the cooling curve, all the necessary plateaus are identified by a name or abbreviation. The identification of the main points and their meaning are, following **Figure 15** and **Figure 16**:

- **T_{Liq}**: Liquidus temperature, corresponding to the first maximum of the 1st derivative and to the first zero at the 2nd derivative;
- **TEu_{Low}**: Low eutectic temperature is the minimum temperature measured before the eutectic reaction and corresponds to the first zero at the 1st derivative before the eutectic point;
- **T_{Eut}**: Eutectic temperature, corresponding to the local maximum in the 1st derivative curve and zero at the 2nd derivative;
- **TEu_{Up}**: Maximum temperature measured in eutectic reaction and corresponds to the first zero at the 1st derivative after the eutectic point;
- **T_{sol}**: Solidus temperature is the point of the end of solidification, characterized by a minimum in the 1st derivative curve.

The curve only shows the section between the beginning and the end of solidification because it is in this cooling stage that the graphite morphology is defined. After the endpoint of solidification, only the nature of the matrix is changed because of the transformation of austenite into pearlite and ferrite.

Although, if the cooling curve registration is taken up after the end of the eutectoid reaction, which might take several minutes, there is a chance to correlate these arrests and inflections points in that region with the ration pearlite versus ferrite.

2.4.3. Solidification Morphology

There are three solidification morphologies of the stable eutectic of cast iron alloys: (1) hypoeutectic in which the first plateau corresponds to the beginning of austenite precipitation and the second larger one, to eutectic reaction, (2) hyper-eutectic in which

the first arrest, commonly recalescence, corresponds to the precipitation of pro-eutectic graphite. The second arrest corresponds to eutectic reaction, (3) eutectic which only has one big arrest as shown in **Figure 17** [3].
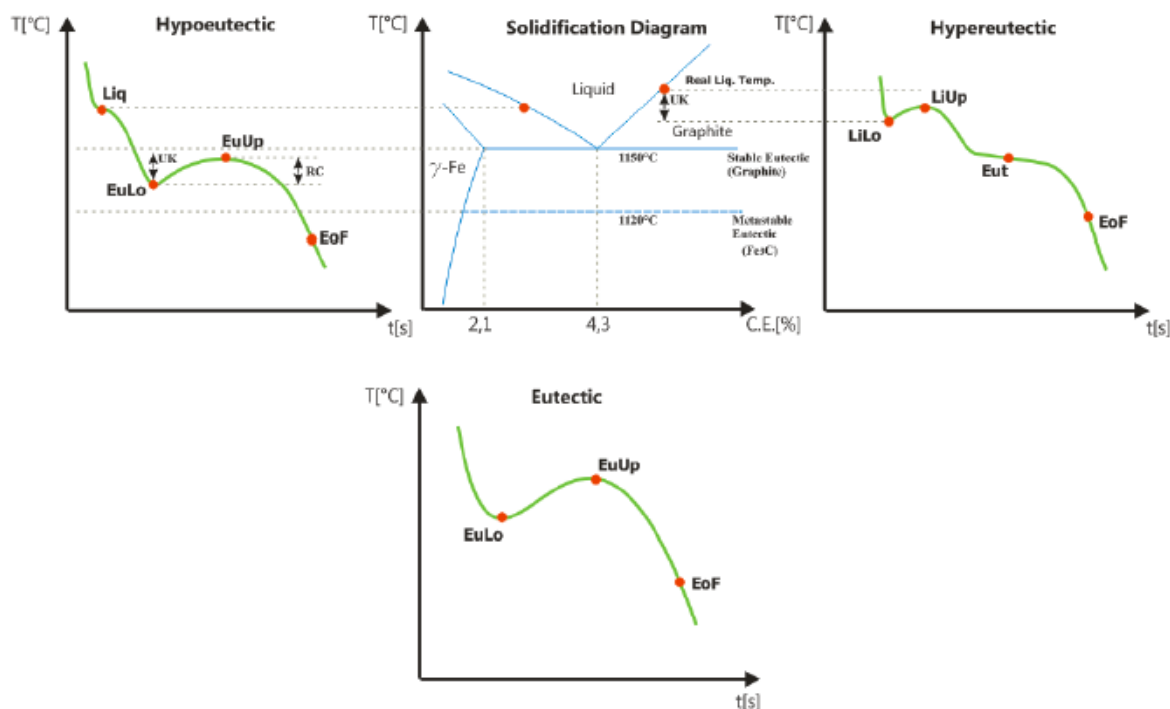
Figure 17. Illustration of the representative shape of the solidification curves and suggested classification for hypoeutectic, eutectic and hyper-eutectic solidification morphologies [3].

The eutectic solidification often occurs with a supercooling (T_{liq}- TEu_{low}=0). Carbide precipitation is characterized by a very low T_{eu} below a critical temperature during eutectic reaction and a flat eutectic plateau. In addition, the end of the solidification of the cooling curve is characterized by a rounded shape.

2.4.4. Evaluation of Inoculation in the Thermal Analysis Curves

Figure 18 presents eleven cooling curves, all from the same base iron melt, treated using the nodularizing and inoculant wires. The first cooling curve of the melt, on the left, is a solidification curve without post-inoculation treatment, while the following curves, have been inoculated with different inoculants, always in the same proportion, or percentage of addition in the form of late addition, in one of the chambers of the closed cartridge [3].
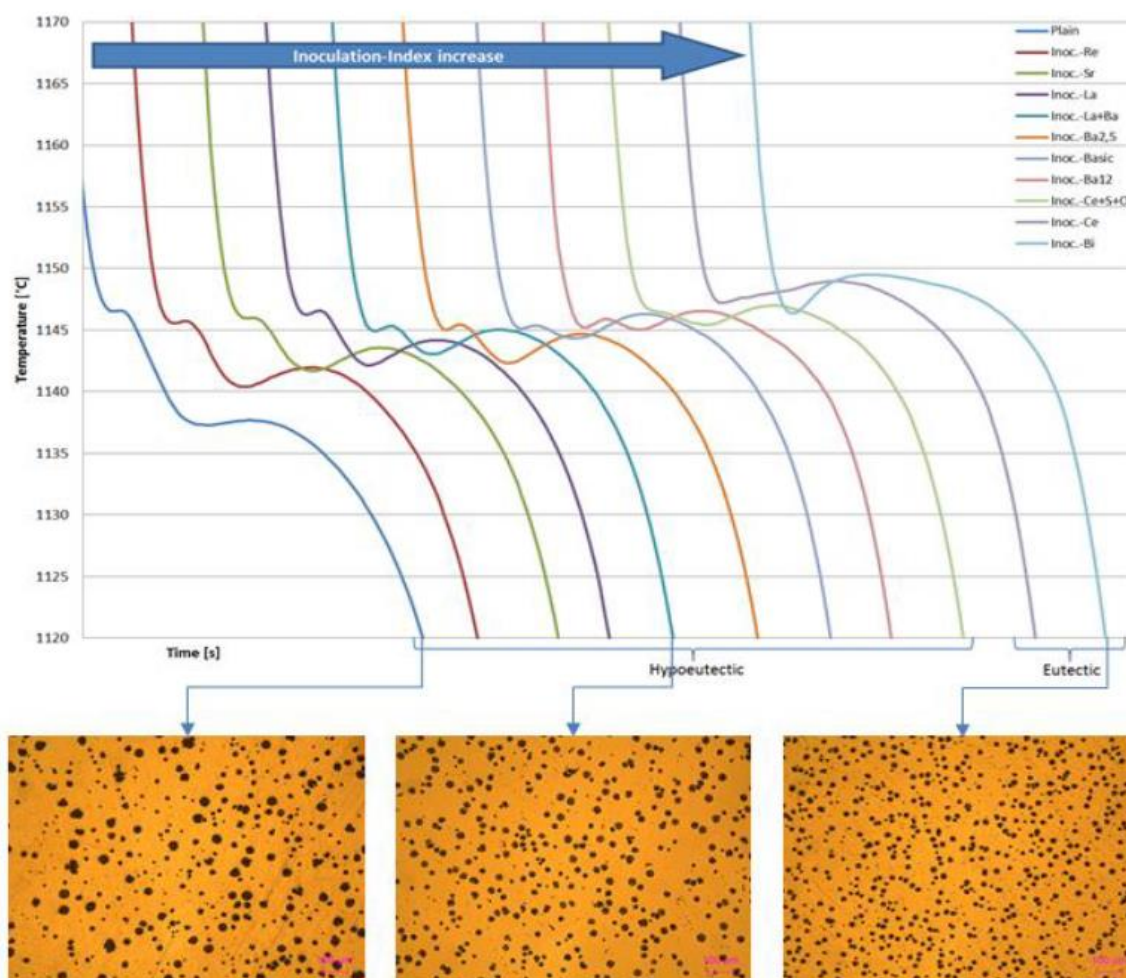
Figure 18. Representative curves are showing the influence of the different inoculants on the solidification morphology [3].

Through the measurement of the undercooling of the cooling curve on the eutectic plateau, it is possible to forecast if a melt was properly inoculated or not. According to the principles of heterogeneous nucleation, the presence of available nuclei sites in the melt (inoculation) reduces the required amount of energy to start nucleation, which affects the magnitude of the undercooling [3].

Such effect is visible on **Figure 18**, where, as the inoculant potential on the melt increases due to the use of more powerful inoculants, the undercooling is progressively reduced and therefore the temperature difference between the liquidus and the eutectic low temperature is also reduced.

Once the eutectic low temperature equals the liquidus temperature, the solidification morphology of the cooling curve changes and goes from hypoeutectic to eutectic [3], although the final chemical composition of the melts were kept constant and hypoeutectic.

2.4.5. Prediction of Graphite Density and Shape

Once cooling curves are sensitive to the phenomenon of nucleation and growth of graphite, it is possible to predict the graphite density, nodularity or precipitation of carbides, through parameters of thermal analysis and the morphology of the cooling curve.

The precipitation of carbides is relatively predictable by observing the morphology of the cooling curve. An un-inoculated melt, with the precipitation of carbides, is characterized by having a flatter eutectic plateau, often without any recalescence, more or less near the metastable eutectic temperature, as represented in **Figure 19 [3]**.

On the other hand, the addition of inoculant will prevent the precipitation of carbide promoting graphite precipitation and will make the curve gain recalescence, due to the release of latent heat of solidification of graphite nucleation and growth, and the eutectic reaction plateau will rise in temperature. The curve with a higher inoculation state indicates a microstructure with higher particle density. The effect of inoculant's fading will lower the inoculation potential and the particle density will decrease [3].
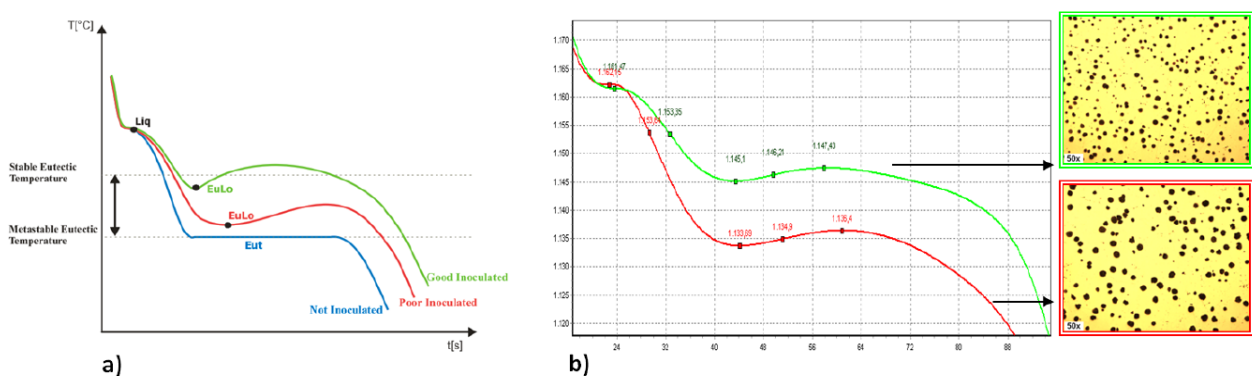
Figure 19. a) Illustration of the melts inoculation influence in the cooling curves; b) real cooling curve display showing the difference between a cooling curve with low inoculation (red) and with high inoculation (green) state and respective micrographs [3].

Nodular cast iron melts with good nodularity are characterized by having small recalescence. As nodularity decreases, the eutectic recalescence tends to increase, as presented in **Figure 20** [3].
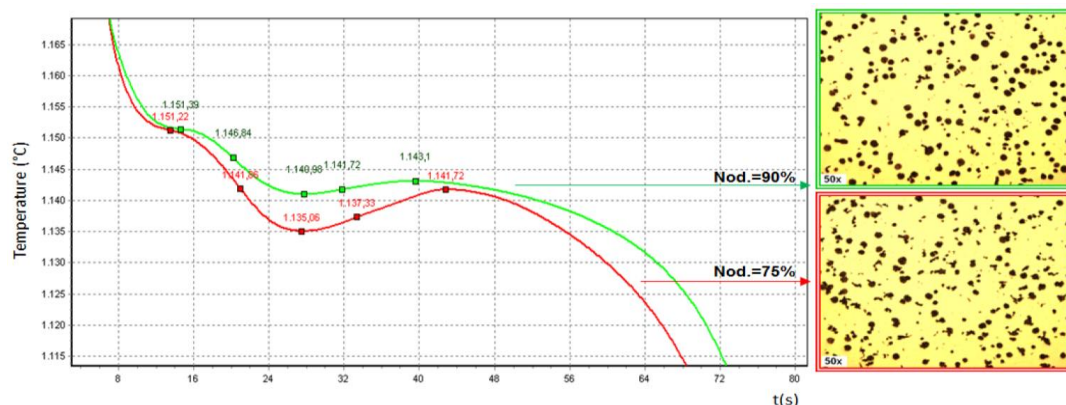
Figure 20. Solidification curves for nodular cast iron, from closed double chamber cups, with high and lower nodularity [3].

3. EXPERIMENTAL PROCEDURE

One of the main purposes on the application of thermal analysis techniques is to get information of the solidification sequence and relate it to characteristics of the microstructure while the melt is solidifying, before any microstructure analysis could be made.

In this work, the fading behaviour of two inoculants have been tested and compared, using both thermal analysis techniques, with two types of cartridges, one common open cup and a more recent closed cup with two isolated spherical chambers, and was also cast a step casting, to compare. Samples were taken after 1, 10 and 20 minutes after inoculant addition, for fading resistance evaluation.

3.1. Molten Metal Processing

The induction furnace was charged in the usual way with 275 kg of cast iron returns (Holbyv base), 0.9 kg of silicon metal and 2.6 kg of graphite. The cast iron returns (16 kg each parts) were stacked into the furnace, and the two other materials were filled into the voids between the parts. Excess cast iron was put on top as an extra charge. When the melts reached 1500°C, the first samples were taken for chemical analysis. When the chemical composition of the final base iron was reported, it was adjusted the base iron to the specified target analysis.

After melting and adjusting the chemical composition, the ladle was preheated by overpouring the iron from the furnace several times, until the ladle was sufficiently warm. During this practice, the carbon was monitored, and extra graphite was added if needed.

The melt heated up to 1520°C (2768°F) was tapped into a preheated treatment ladle. Upon tapping, a new set of samples were taken to chemical analysis.

3.2. Nodularization Treatment

For the nodularization treatment, the 280 kg iron batch was treated in the preheated conventional Tundish-cover method using 1.20 wt% of a magnesium-nodularizing (3.36kg), with a 5.89% magnesium-containing ferrosilicon alloy, placed on the bottom of the ladle in a special chamber and covered by 2 kg of oil-free and dried steel chips.

After the Mg-treatment was complete, the liquid was then poured into smaller ladles for the inoculation treatment.

3.3. Inoculation Treatment

The melt was used to compare fading resistance of two inoculants: Ba-FeSi inoculant, with a 2.60% of barium-containing ferrosilicon alloy and Ca-FeSi inoculant with 1.20% of calcium and 1.40% aluminium-containing ferrosilicon alloy, each with 0.3 wt% addition. The composition and grain size distribution of these alloys are shown in **Table 2.**

Table 2. Chemical composition and grain size distribution of treatment alloys

Element	Grain Size Distribution	%Si	%Mg	%Al	%Ca	%Ba	%REE
Mg-FeSi	1 - 10 mm	48.6	5.89	0.73	1.45	--	0.26
Ba-FeSi	0.7 - 3 mm	73.1	--	1.50	1.40	2.60	--
Ca-FeSi	0.7 - 3 mm	76.0	--	1.40	1.20	--	--

Before the trial start, the same amount of inoculant was weighed for each ladle. For both Ba-FeSi and Ca-FeSi inoculants, 96 g were measured and placed on the bottom of each ladle.

For the inoculation treatment, it was followed by the trial's procedure as illustrated in **Figure 21**.
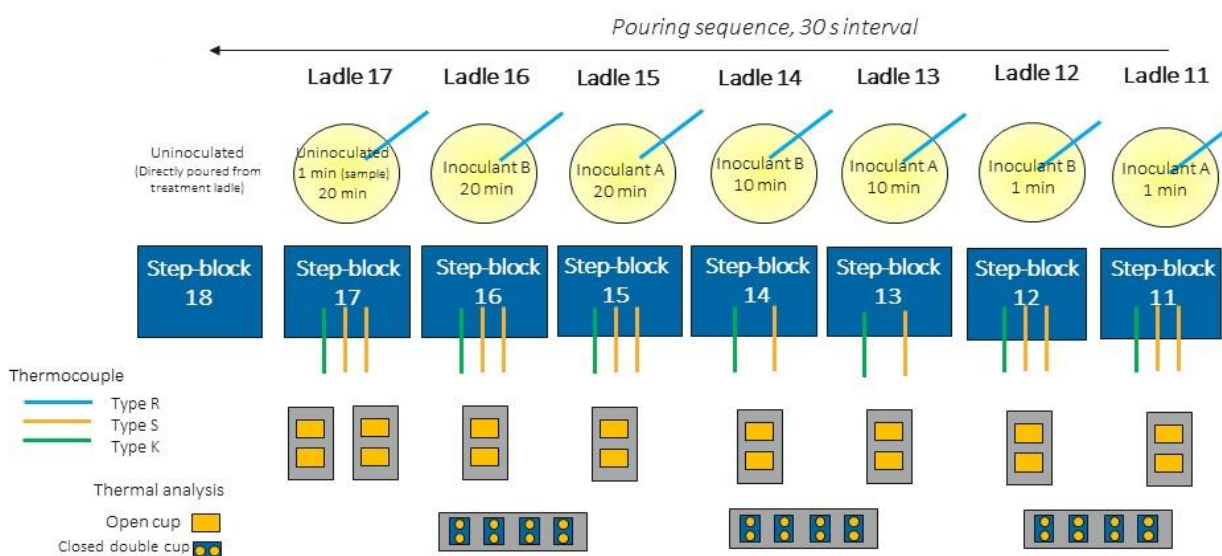
Figure 21. Scheme of the layout and connection of the thermal analysis system used for the experiments Inoculants: A: Ba-FeSi inoculant; B: Ca-FeSi inoculant.

The Mg-treated melt was split in 8, of which the first seven were poured into secondary 32 kg "pouring ladles". The remaining treated melt was poured into 1) a 6 kg sampling spoon and 2) cast directly into the mould.

For the ladle inoculation, in the first six pouring ladles, the designated inoculant was deposited, at the beginning of the trial, at the bottom of each ladle prior to filling. To compensate the silicon in the inoculants, Si-metal was added to ladle 17, as well as the sampling spoon and to the mould of the Mg-treated melt which was poured directly to the moulds.

Hence, the melt in the first six pouring ladles was inoculated, whereas the last pouring ladle and the sampling spoon and the directly filled mould was just Mg-treated, but un-inoculated.

The pouring temperatures for each ladle are shown in **Table 3**. As expected, pouring temperatures decrease with the increase of holding time.

Table 3. The temperature of the melt in each ladle before pouring

		Tcasting ºC
Ba-FeSi 1 min	Ladle 11	1389
Ca-FeSi 1 min	Ladle 12	1396
Ba-FeSi 10 min	Ladle 13	1321
Ca-FeSi 10 min	Ladle 14	1311
Ba-FeSi 20 min	Ladle 15	1259
Ca-FeSi 20 min	Ladle 16	1246

3.4. Pouring Conditions

In the melt, pouring ladles 11, 13 and 15 contained Ba-FeSi inoculant, whereas pouring ladles 12, 14 and 16 contained Ca-FeSi inoculant. The pouring ladles were kept at 3 different holding times before sampling and casting them into sand moulds: (a) - 1 minute for pouring ladles 11 and 12, (b) - 10 minutes for pouring ladles 13 and 14, and finally (c) - 20 minutes for pouring ladles 15, 16, and 17 (un-inoculated iron).

Pouring times were taken using a stopwatch. In a sequence of 30 seconds, the melt was poured into the ladles and after waiting the required time the melt was then poured into the open standard QuiK-Cup®, into the dual chamber Therm-O-Stack® cup, and lastly into the step-blocks. In addition, it was taken a dip sample for chemical analysis.

About the step-blocks, the dimensions of the sand moulds had of 2.5, 5, 10, 20 and 40 mm, as shown in **Figure 22**.
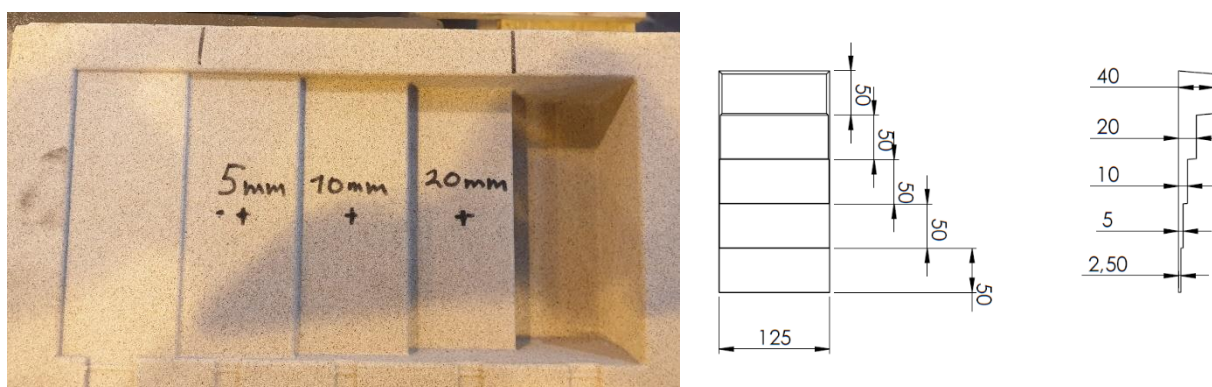
Figure 22. Geometry of step castings.

The thermal analysis standard open cups (**Figure 23**), also known as QuiK-Cup®, is produced by the company Heraeus Electro-Nite [25]. The thermal analysis dual-chamber cups, which is also known as Therm-O-Stack® (**Figure 24**), is produced by the same company [3]. The cooling curves of the base iron melt and the melt after inoculation treatment were done with open and closed cups. There is a fundamental difference between these two cups: in the closed-cup the amount of metal is always constant, so the

sensible heat is always constant, and in the regular open cup, the amount of metal may, and usually, fluctuates from sample to sample [26].
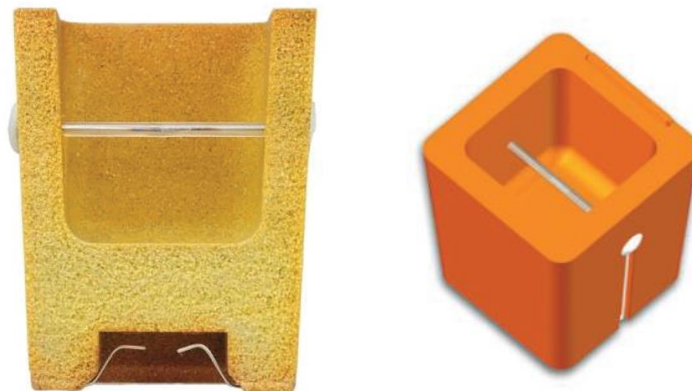
Figure 23. Standard open cup with disposable thermocouple, also known as QuiK-Cup® [25].
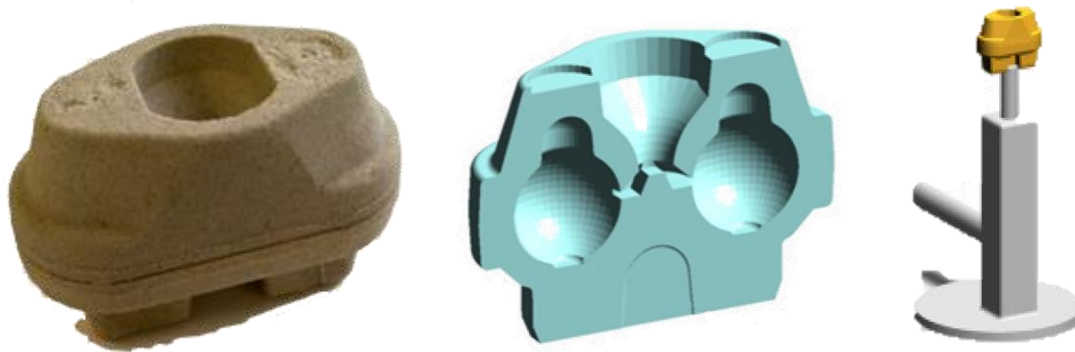
Figure 24. Dual-chamber thermal analysis cups, which is also known as Therm-O-Stack® [3].

For the step block, type S thermocouple (Platinum - Platinum /10% Rhodium) was used on the 20 and 10 mm sections, whereas an extra thin type K thermocouple (Chromel®-Alumel®) was used in the 5 mm section, for quicker response than regular ones, as shown in **Figure 25**. Both types were calibrated and custom made by Elkem technical staff [27, 28].
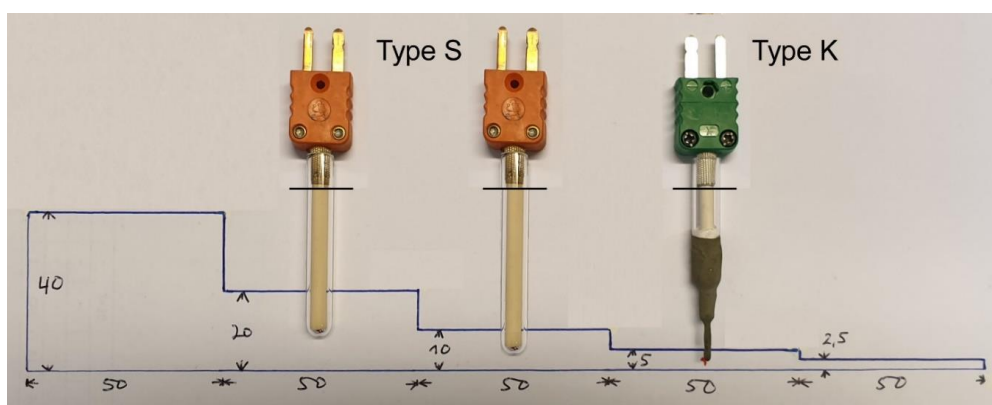
Figure 25. Thermocouple type and positioning in the step block.

3.5. Thermal Analysis Equipment and Software

All thermocouples were connected to a Data Translation DT8874 MEASURpoint Ethernet data acquisition system which provides simultaneous analogue input along with any combination of isolated temperature, resistance and voltage measurements [29]. The software QuickDAQ acquires the temperatures and saves them all in a database on a computer, that is subsequently exported to Excel, for further data evaluation and treatment.

The thermal analysis system can be configured for various thermocouple types, which achieves a rate of 10 Hz.

The data treatment was the same for all values recorded by each thermocouple. In each thermal analysis cup, first, the data was filtered to contain only the beginning of the pouring temperature (maximum recorded temperature) until the end of the solidification. The highest temperature was thus defined as the zero points of the curve.

After obtaining the cooling curve, the solidification curve was smoothed by using a mathematical approximation function developed by Professor Manuel Oliveira to reduce noise and to calculate the 1st and 2nd derivative.

 The identification of the main plateaus and inflection points were done with the data evaluation of the 1st and 2nd derivative.

3.6. Sample Characterization Methods

3.6.1. Chemical Analysis

For the chemical composition of the alloys, liquid samples were collected from the melt before and after inoculation treatment. After solidification, the samples, in coin shapes, were taken for chemical analysis.

The chemical analysis of the alloys has been carried out by Elkem Technology, following the quality standard: ISO 9001 - Quality Management, certified by trademarks DNV GL®.

For evaluation of chemical elements, ELTRA combustion technique was used for measuring carbon and sulphur contents (Eltra CS-2000), while the ARL iSPARK 8860 Spectrometer was used to measure the contents of the other metallic elements.

3.6.2. Optical Microscopy

The samples from the thermal analysis cup were identified after sampling had been made, by a reference of holding time as well as the indication of the additive at each chamber.

After cleaning the sand from the sample's surface, the two spheres of the same cup were separated from the in-gate system and cut by their vertical centre line.

The evaluation of the microstructure samples from the step casting was made by cutting across their vertical centre line passing though the thermal centre of the casting for each section.

3.6.3. Standard metallographic preparation

The samples, after being cut, were prepared using equipment from STRUERS named TEGRA. The preparation was done by using a diamond pad of 80 mesh and 220 mesh to level the samples. The diamond pad was then replaced by a polishing cloth for the mechanical polishing. A diamond suspension was successively added, from 9 µm to 1 µm, to aid in the polishing.

Ductile iron microstructure quantification at Elkem Technology was carried out on a Zeiss light microscope, Axioplan 2, with automatic stage controller at a magnification of 100x. The digital camera gave an image resolution of 0.68 µm/pixel. The images are acquired by systematic random sampling, 36 images, and 25 of them are manually chosen for image analysis in Image-Pro Plus software. Samples were examined both in polished condition (1 µm finish) and etched with Nital.

4. RESULTS AND DISCUSSION

4.1. *Chemical Composition of Raw Materials and Treatment Alloys*

Table 4 contains the information of the various combinations of inoculants used in the present experiment. The samples were identified by reference of holding time as well as the indication of the inoculant added to the melt. For chemical analysis it was taken two samples: Samples A before being poured into the moulds and Samples B were taken after the metal was poured into the moulds.

Table 4. Overview of samples. Experimental trial setup

Sample ID	Iron	Treatment		Holding time (minutes)
		Mg-Treatment	Inoculant	
FB.01	Initial base iron	None	None	None
FB.02	Final base iron			
FB.10	Mg-Treated iron	Mg-FeSi nodulizer	None	None
BA1.A,B	Inoculated iron		Ba-FeSi	1
CA1.A,B			Ca-FeSi	1
BA10.A,B			Ba-FeSi	10
CA10.A,B			Ca-FeSi	10
BA20.A,B			Ba-FeSi	20
CA20.A,B			Ca-FeSi	20
UN1.A,B	Mg-Treated iron, Si-compensated		None	1
UN20			None	20

The samples were identified as follows:
- Un-inoculated is identified as UN,
- melt inoculated with (Ca, Al)–inoculant is identified as CA.
- and melt inoculated with Ba-inoculant is identified as BA.

These melts were poured after 1, 10 and 20 minutes of holding time therefore are labelled UN1, UN20, CA1, CA10, CA20, BA1, BA10, BA20.

In **Annexe A**, there are the full chemical composition results obtained for the melts before and after treatment, while in **Figure 26, Figure 27** and **Figure 28** are shown CE, Mg and S contents of all the samples.
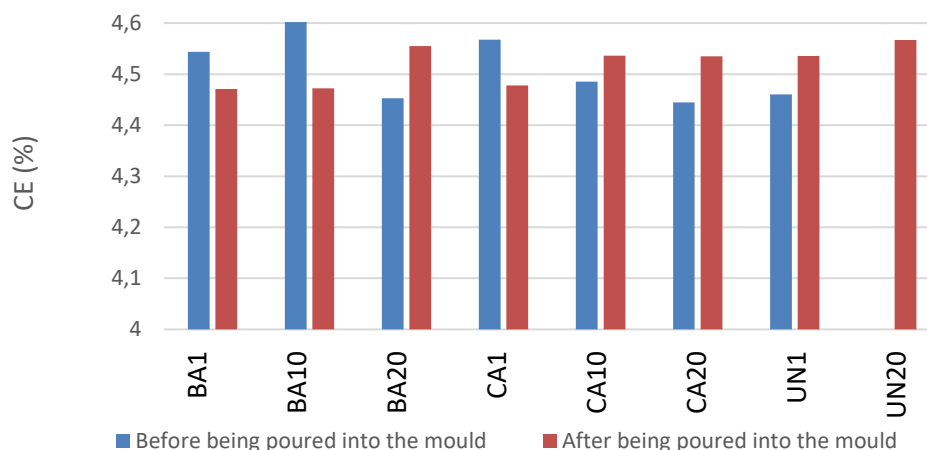
Figure 26. Variation of % Carbon Equivalent (CE) of each sample.

When comparing the chemical analysis samples before casting into the moulds with the samples after casting into the moulds, there is a decrease in the CE content for BA1, BA10 and CA1 samples, whereas for samples BA20, CA10 and CA20 there is an increase in CE content.

Taking a closer look just to the samples of the melt after being poured into the moulds, CE is "approximately" constant in the Ba-inoculated samples, despite of having a much lower CE content compared to the other samples. The Ca-inoculated samples presents a similar behaviour compared to Ba-inoculated samples. CE is also "approximately" constant, but CA1 sample has a lower CE than the others Ca-inoculated samples.

CE of sample before and after pouring should have been the same. Since it was not the case and nothing had been added to the molten iron, there should have been some chemical homogenization, such as inoculant dissolution and so Si should have increased.

Finally, the chemical analysis suggests that all the melts are hyper-eutectic.
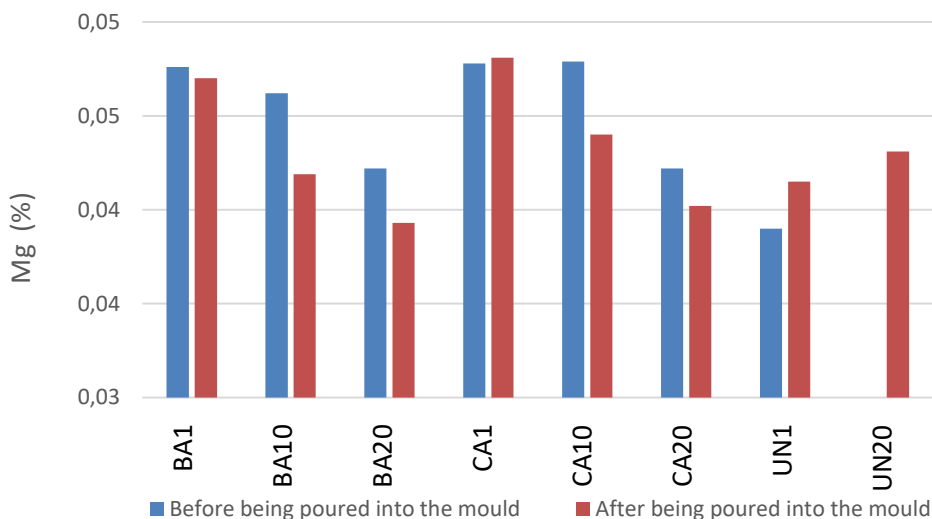
Figure 27. Mg content for each sample.

Figure 27 shows that Mg content change slightly during pouring into the moulds. The behaviour in the BA and CA samples is expected. All inoculated samples have the Mg content within the expected values [0.03≤%Mg ≤0.055], however its content decreases with time due to Mg's fading.

Observing only the red bars, in the un-inoculated samples, there is an unexpected increase of the Mg and CE over time, which indicates that it was Mg-FeSi alloy that was later dissolved since the UN20 melt came from the bottom of the Tundish cover. This late dissolution led to Mg and Si being incorporated into the iron melt thus increasing CE and Mg.
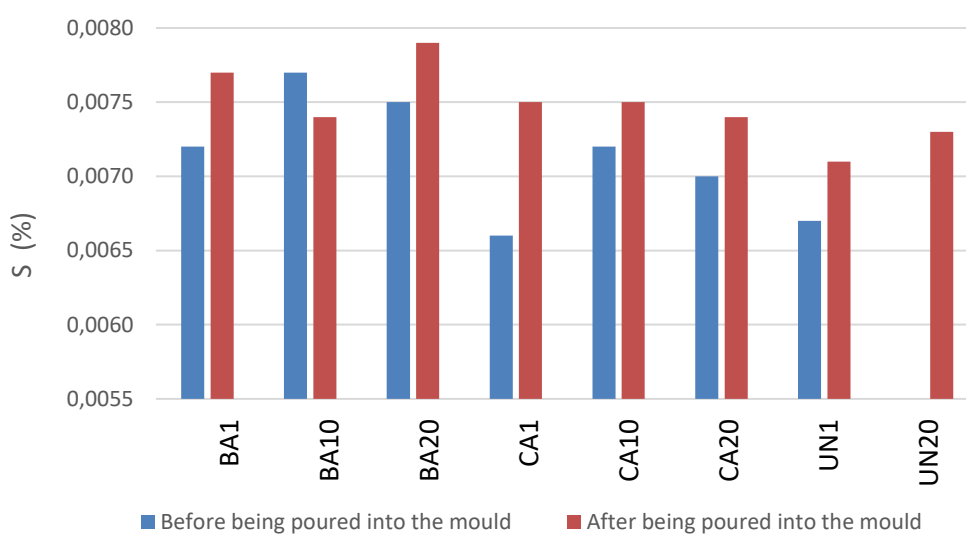
Figure 28. S content for each sample.

The sulphur content in the initial base metal (shown in **Table 5** of **Annexe A**) and after treatment shows that the sulphur content was reduced from 0.011% to 0.007% approximately.

S content is "approximately" constant in the Ca-inoculated samples, while the content of S in the Ba-samples varies significantly. In addition, all the samples present S content below the reference values [0.008≤ %S ≤0.015] [1, 7, 8].

4.2. Microstructure, Nodule Count, Size Distribution and Cooling Curves

The results are divided into three parts. In the first part of the results, an analysis of the cooling curves from dual cups will be approached to make a relationship with the microstructural parameters.

In the second part of the results, a comparison of the thermal analysis parameters of open cups with dual cups will be made, considering the chemical composition, to evaluate which of the cartridges is more reliable to anticipate and predict in real-time the microstructure of the melt.

Lastly, a comparison of the thermal analysis parameters of the step castings with dual cups was going to be made to analyse the effect of the inoculation efficiency, however most of the registered cooling curves of the step casting does not allow their use and analysis so it was not possible to compare directly any of the cooling curves of the sections of the moulds cast with the cooling curves.

4.2.1. Correlation of Thermal Analysis Results with the Microstructure of the Dual Cups

The solidification curves from thermal analysis dual close cups are presented in **Figure 29** and **Figure 30**, while in **Annexe B**, the data obtained from the dual thermal analysis cups are summarized in **Table 6**.
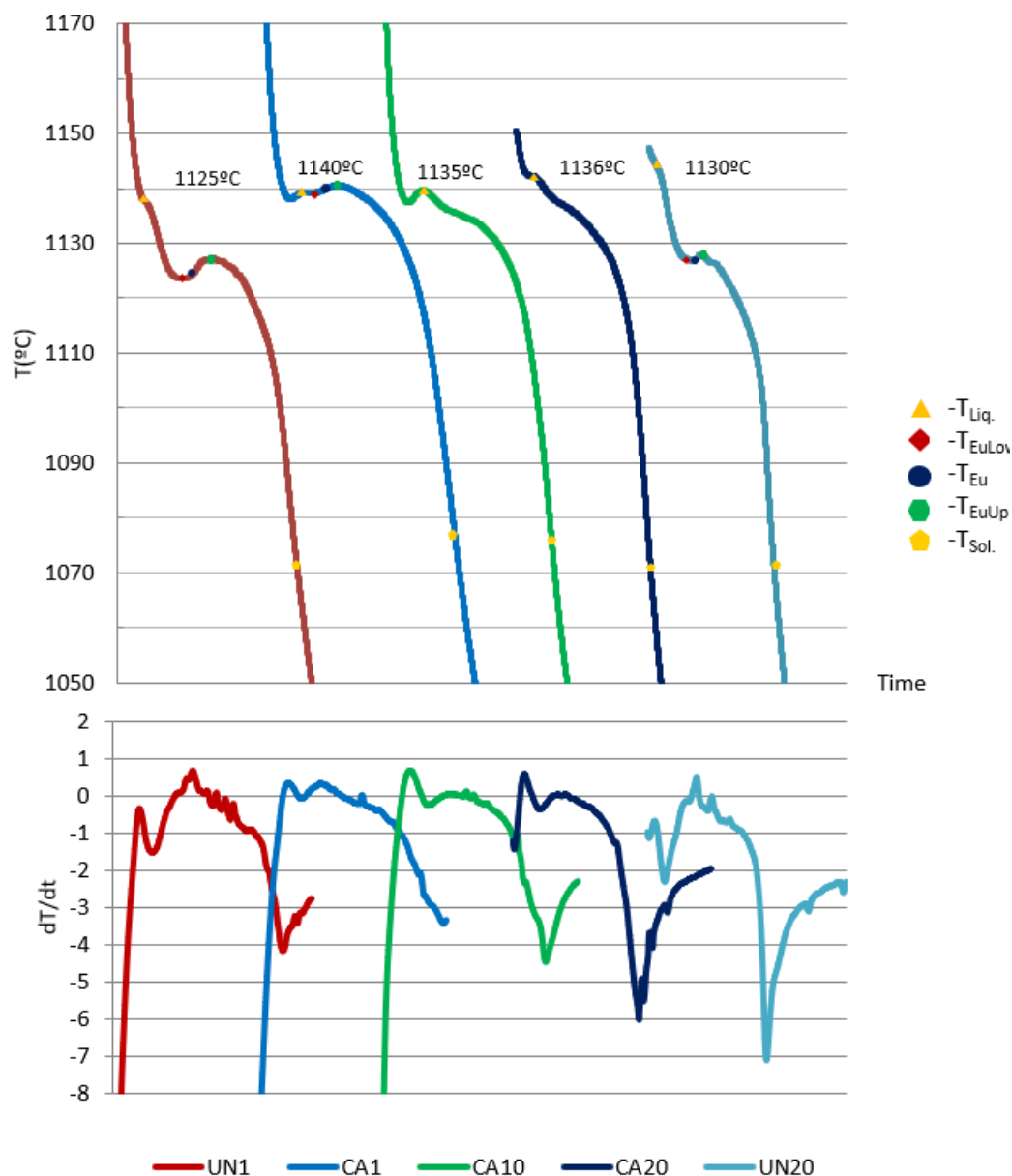
Figure 29. Solidification curves obtained during trials from the dual cups' chambers for Ca-inoculated samples.

In **Figure 29**, the cooling curves of the un-inoculated melts present the hyper-eutectic solidification morphologies where Liquidus temperature of the UN20 sample is slightly higher than UN1, almost 2°C, which means that there has been some gain of either on C or Si or even both which chemical composition confirms. It shows an increase of C and Si when compare the UN1 sample with UN20.

All the cooling curves of the Ca-inoculated samples have a hyper-eutectic morphologies solidification. It is visible that TEu_{Low} is much higher on the inoculated samples than the un-inoculated samples, which means that the un-inoculated samples might have carbides, which is the case (see **Figure 41** in **Annexe C**).

The cooling curve corresponding to the CA1 melt presents a small liquid plateau, while the eutectic plateau has a longer time extension and higher recalescence (TEu_{Up}) which means that the amount of precipitated graphite was enough to raise the temperature. After 10 minutes, the time's extension of the eutectic plateau decreases

from almost 17 seconds to 13 seconds, as does TEu$_{Low}$ and TEu$_{Up}$ as result of fading effect of the Ca-inoculant.
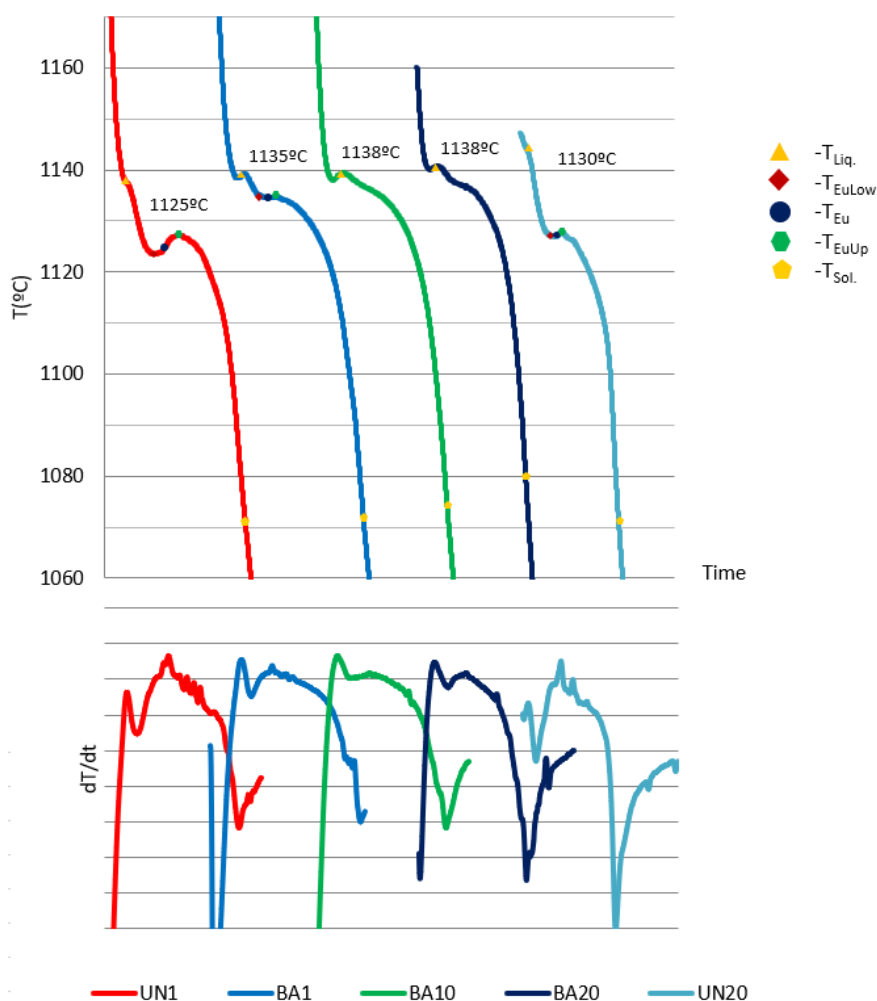
Figure 30. Solidification curves obtained during trials from the dual cups' chambers for for Ba-inoculated samples.

Figure 30 compares the un-inoculated cooling curves with the Ba-inoculated ones and it is also visible that TEu$_{Low}$ is much lower than the TEu$_{Low}$ from Ba-inoculated cooling curves, which once again reinforces the presence of carbides on the un-inoculated samples, as shown in **Figure 41** in **Annexe C.**

The cooling curves of Ba-inoculated melts have the same tendency as those inoculated with calcium: the plateau becomes shorter with holding time: the eutectic reaction time goes from 20 seconds to approximately 11 seconds. It is also visible that the distance between the two plateaus decreases with increasing time, due to the increase of TEu$_{Low}$ and TEU$_{Up}$, so no decrease in TEu$_{Low}$ and TEu$_{Up}$ could be observed. In fact, the cooling curves of the BA10 and BA20 are homologous, which means that Ba-inoculant has a better fading's resistance than Ca-inoculant.

For a better analysis of the cooling curves, TEu$_{Low}$ and TEU$_{Up}$ of each sample are shown in **Figure 31.**
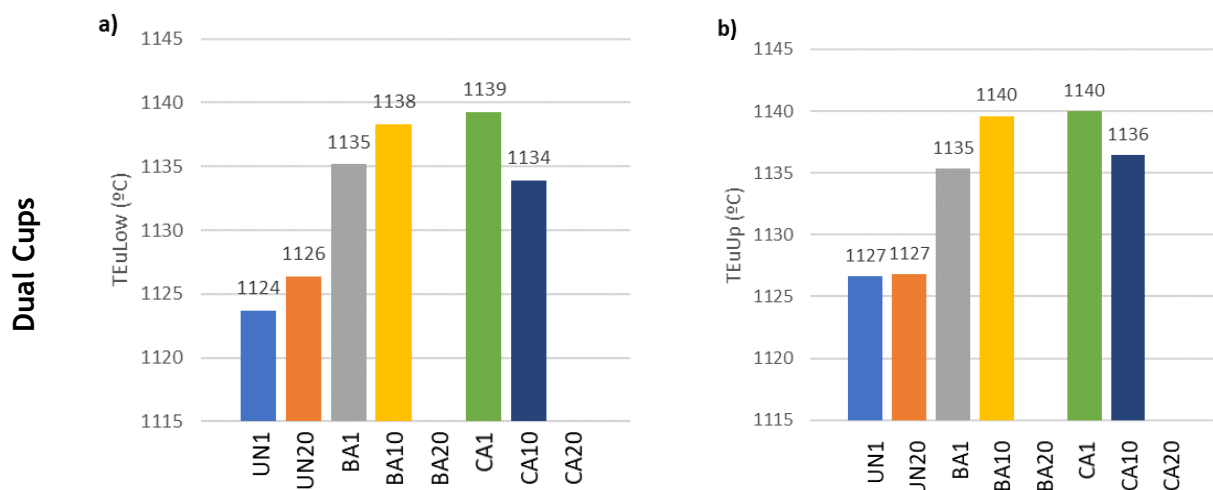
Figure 31. Thermal Analysis parameters for evaluating solidification of the samples a) TEu$_{Low}$ identify on the dual cups thermal analysis curves b) TEu$_{Up}$ identify on the dual cups' thermal analysis curves.

Taking a closer look to the TEu$_{Low}$ and TEu$_{Up}$ values of each sample, **Figure 29** shows that TEu$_{Up}$ decreases 4°C from the cooling curve of the CA1 sample to the CA10 sample and apparently it decreases even more after 20 minutes by looking to the cooling curves (however it wasn't possible to identify TEu$_{Low}$ and TEu$_{Up}$ for the 20 minutes samples).

CA1 melt has the highest TEu$_{Low}$, so Ca-inoculant has high immediate effectiveness however, the TEu$_{Low}$ values also decrease with holding time as it can be seen in CA10 melt which means that the potential nucleation of graphite decreases, as result of fading effect of the Ca-inoculant.

Ba-inoculated melts do not present a decrease in TEu$_{Low}$ and TEU$_{Up}$, TEu$_{Low}$ increase almost 3°C and TEU$_{Up}$ increases 5°C from 1 minute holding time to 10 minutes holding time sample, which means that Ba-inoculant has a better fading's resistance than Ca-inoculant.

For better evaluation of the efficiency and fading time of the inoculants, microstructure parameters, such as nodularity, nodule count and size distribution of the nodule's graphite, were analysed. The microstructure for each sample is presented in **Annexe C**, while **Table 7** in **Annexe B** show more details about the microstructure parameters of dual cups.
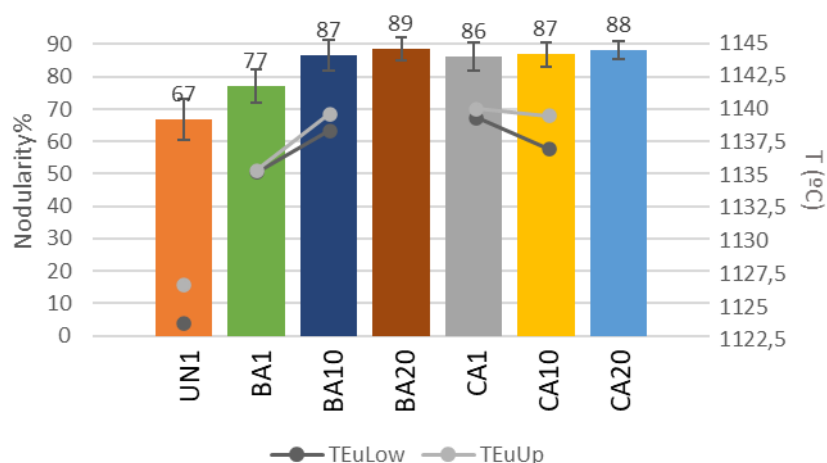
Figure 32. Microstructure parameter: nodularity of graphite on each sample in the dual cups.

Figure 32 shows the average nodularity values and it is observed that nodularity increased with holding time for both inoculants, mainly in Ba-inoculated samples, due to the temperature effect. In general, all the inoculated samples present a nodularity of over 80%.
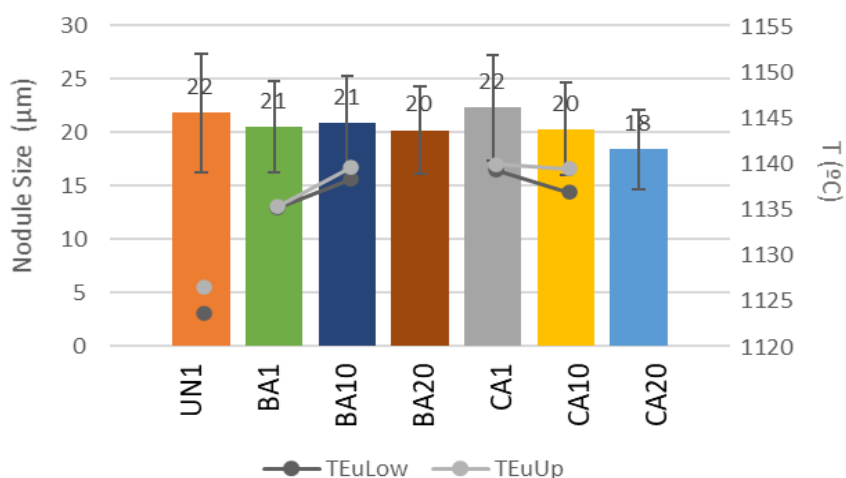
Figure 33. Microstructure parameter: Average nodule size of graphite on each sample in the dual cups.

Figure 33 shows the average nodule size values. It shows that nodule size decreases slightly with time for both inoculants. The sample CA20 has the lowest nodule size, with 18±3.8 μm followed by BA20 sample, with 20±4.1 μm. In general, the nodule size of graphite is constant in the Ba-inoculated samples while in Ca-inoculated samples decrease, which isn't the expected, since Ca-FeSi inoculant should have an expected low fading resistance and, as consequence, the nodule size should increase. All the samples present a unimodal size distribution (see **Figure 41** in **Annexe C**).
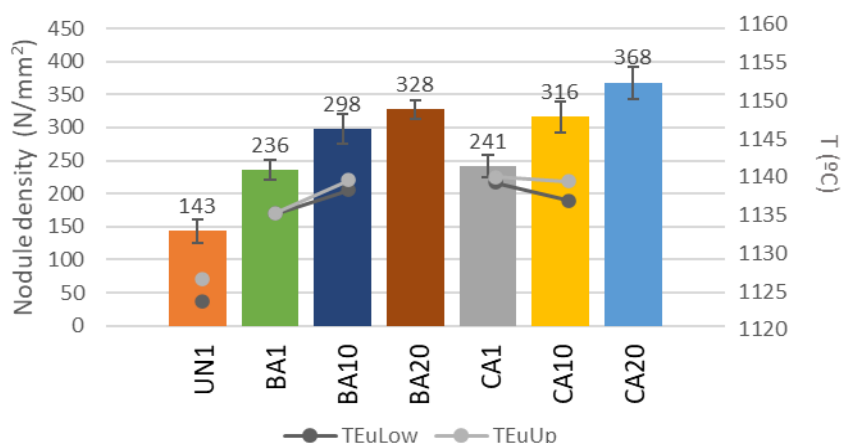
Figure 34. Microstructure parameter: nodule density of graphite on each sample in the dual cups.

Figure 34 shows the average nodule density values for each sample. The sample CA20 has the highest nodule count with 368±24 nodules/mm², presenting even more nodule count than sample CA1. Although the BA samples have a lower nodule count, this number also increases with holding time, which means that the dissolution of the inoculants and cooler liquid melts increase nucleation potential of graphite.

Analysing these three microstructure parameters, these variations can be justified because of the effect of temperature, where colder liquid metal promotes nodule count. In **Table 3** which is included in the experiment procedure, the temperature of the ladles before pouring for 20 minutes holding time has a much lower temperature than the ones which had 1 minute of waiting time (a difference over 100°C). The increase of undercooling is associated with the increased number of the active nucleus in the melt, which increases the potential nucleation of graphite.

It is known that one of the factors which influences inoculation efficiency is the presence of inclusions to promote nucleation sites for graphite and solidification at low eutectic undercooling [1]. Therefore, **Figure 35** shows the inclusion (non-graphite particles) size distribution and the total amount of particles in function of time in the dual cups, while in **Annexe B** in **Table 8** the inclusion size distribution measurements are summarized.
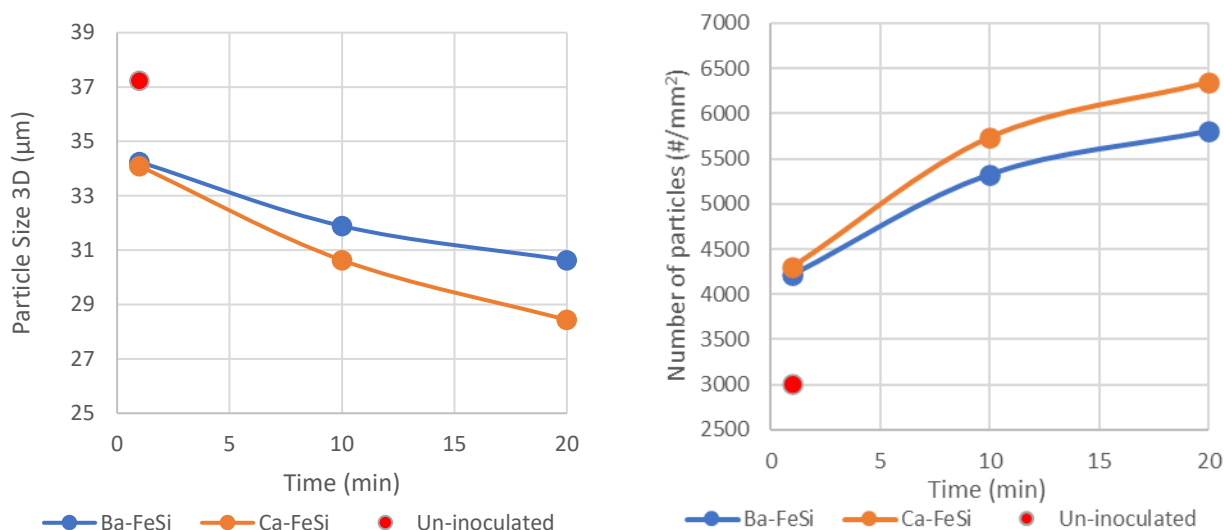
Figure 35. Particle size 3D and the total amount of particles in function of time in the dual cups.

Based on the results obtained, the particle size decreased with time while the number of particles increases. Once again, these variations might be justified because of the effect of decreasing pouring temperature. If pouring temperatures are too low, then more energy is needed to promote coalescing of the particles, so the coarsening process by Ostwald ripening effects is hampered, and therefore particles/inclusions don't grow [16, 30].

Since the dual cups have a constant volume, the sensible heat is the same in all samples and it is possible to predict the microstructure of the samples through the use of thermal analysis technique, explicitly relating the TEu_{Low} and TEu_{Up} to nodule density and size distribution of graphite. Inoculation efficiency is measured by the ability of the inoculant to prevent carbide formation and to ensure a large number of SG aggregates (high nodule count) [24].
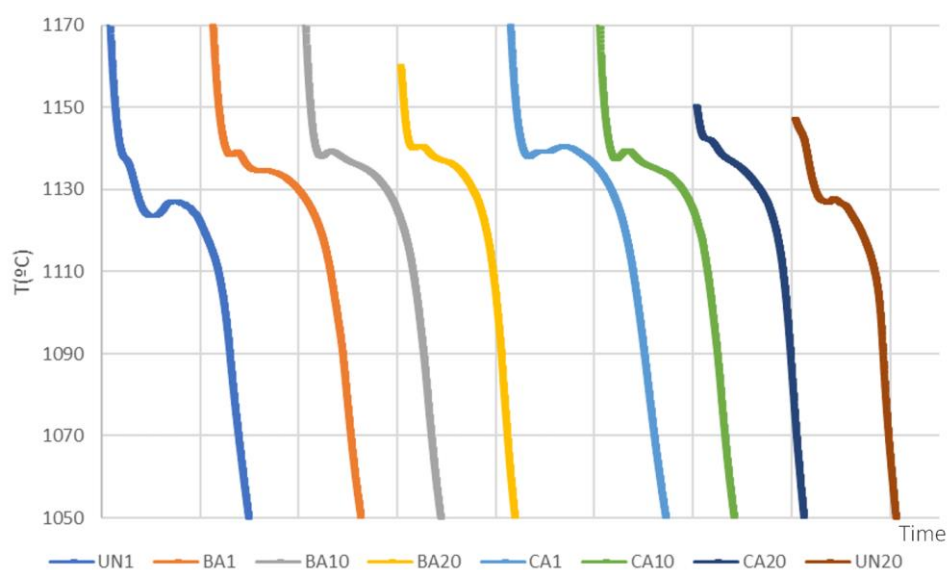
Figure 36. Solidification curves obtained during trials from the dual cups' chambers for both inoculants.

From **Figure 36**, the un-inoculated melt has two very evident plateaus and therefore graphite might show a binomial distribution (large nodules resulting from the precipitation of graphite in the liquidus plateau and smaller eutectic nodules), which according to microstructure results was not the case. All the samples (un-inoculated and inoculated samples) present unimodal size distribution (see **Figure 41** in **Annexe C**).

The results of microstructures show that inoculants prevent carbide formation because no carbide was observed on the inoculated samples. Also, from the thermal analysis results it can be seen that TEu_{Low} increases significantly from an un-inoculated to an inoculated melt.

According to cooling curves from the Ba-inoculated samples, the BA1 sample should also present a binomial distribution, although the nodules wouldn't be as large as the un-inoculated sample because the liquidus plateau is closer to the eutectic plateau, which is the case: nodule size of BA1 sample is lower than the UN1 sample (see **Figure 33**).

Samples BA10 and BA20, which have two close plateaus, present a shorter eutectic reaction time which means that will have more homogeneous and smaller graphite nodules and therefore it is expected an increase of nodule count, which is the case according to **Figure 33** and **Figure 34**.

On the other hand, in the cooling curves of the Ca-inoculated samples, CA1 melt shows a small liquid plateau and a higher TEu_{Low} and TEu_{Up} which means that the amount of precipitated graphite was enough to raise the temperature, therefore nodule count should be higher than the other Ca-inoculated samples.

After 10 minutes, TEu_{Low} and TEu_{Up} of the Ca-inoculated cooling curves decreases, which indicates that in the CA10 and CA20 samples should have fewer graphite nodules and these would be larger, which didn't happen but should be expected, since fading of inoculant decrease the inoculation potential.

Comparing the two cooling curves of the inoculated melts with 20 minutes of holding time, it can be seen that Ba-inoculated samples have a better shape and distribution of nodules than the Ca-inoculated samples, as BA20 cooling curve has a slightly higher eutectic plateau than CA20 cooling curve.

From **Figure 32**, it can indeed be suggested that the nodularity is greater in the BA20 sample than in the CA20. In general, all the inoculated curves suggest a good nodularity since all the inoculated curves are characterized by having small recalescence. With the un-inoculated, a bad nodularity is expected since the curves present a higher recalescence, especially the UN1 curve. In fact, **Figure 32** confirms that all inoculated samples present a good nodularity while the un-inoculated samples do not.

Although not all the predictions made through thermal analysis technique were correct, the dual cups fulfil their function of providing information on the efficiency of inoculation because it is very clear the fading effect in the Ca- inoculated cooling curves and the fading resistance in the Ba-inoculated cooling curves.

4.2.2. Comparison of the Morphology of the Cooling Curves of Dual Cups and Open Cups

The solidification curves from thermal analysis open cups chamber are presented in **Figure 37** and **Figure 38**, while in **Annexe B**, the data obtained from the open cups thermal analysis cups are summarized in **Table 9.**
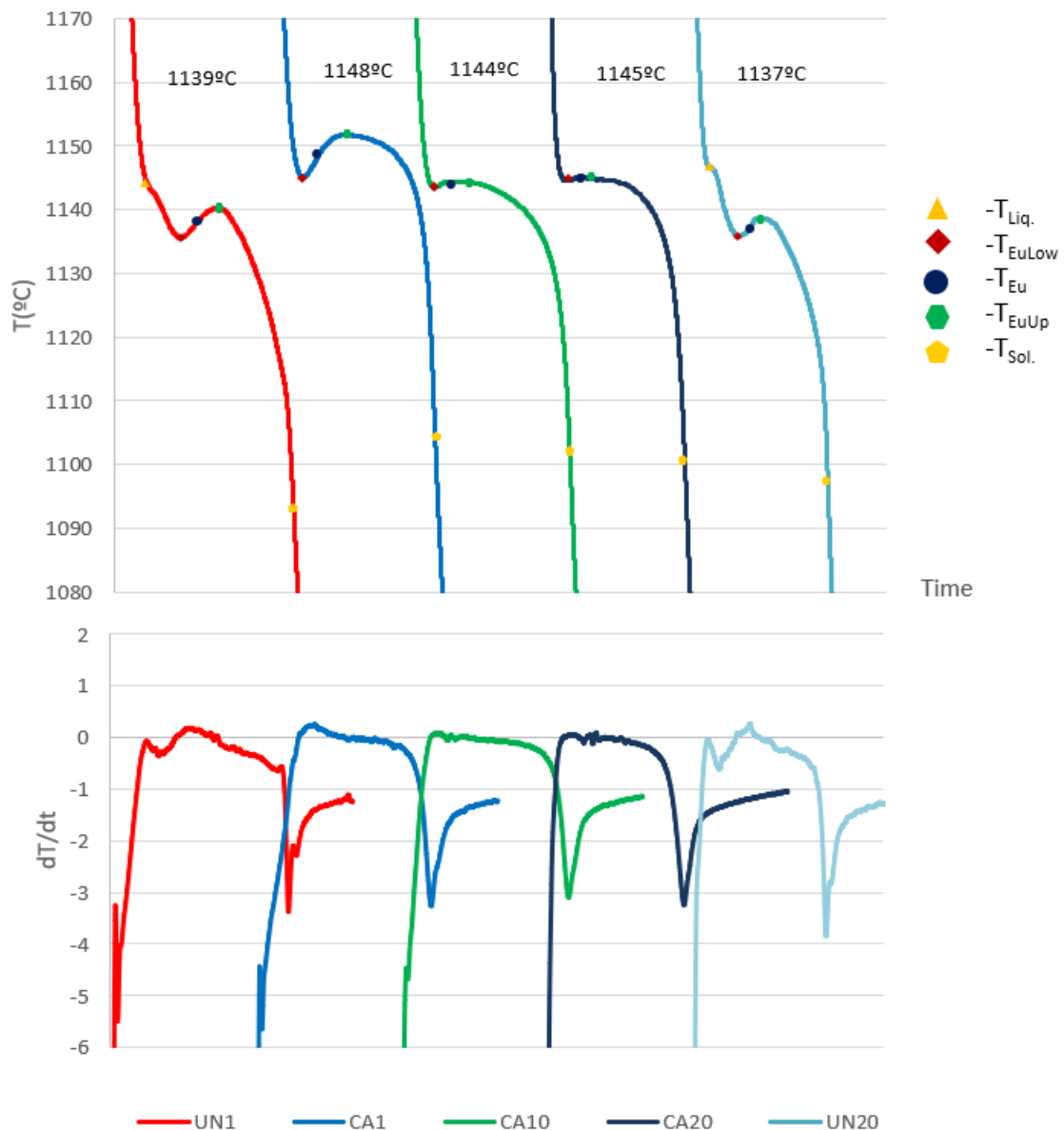
Figure 37. Solidification curves obtained during trials from the open cups' chambers Ca-FeSi inoculant.
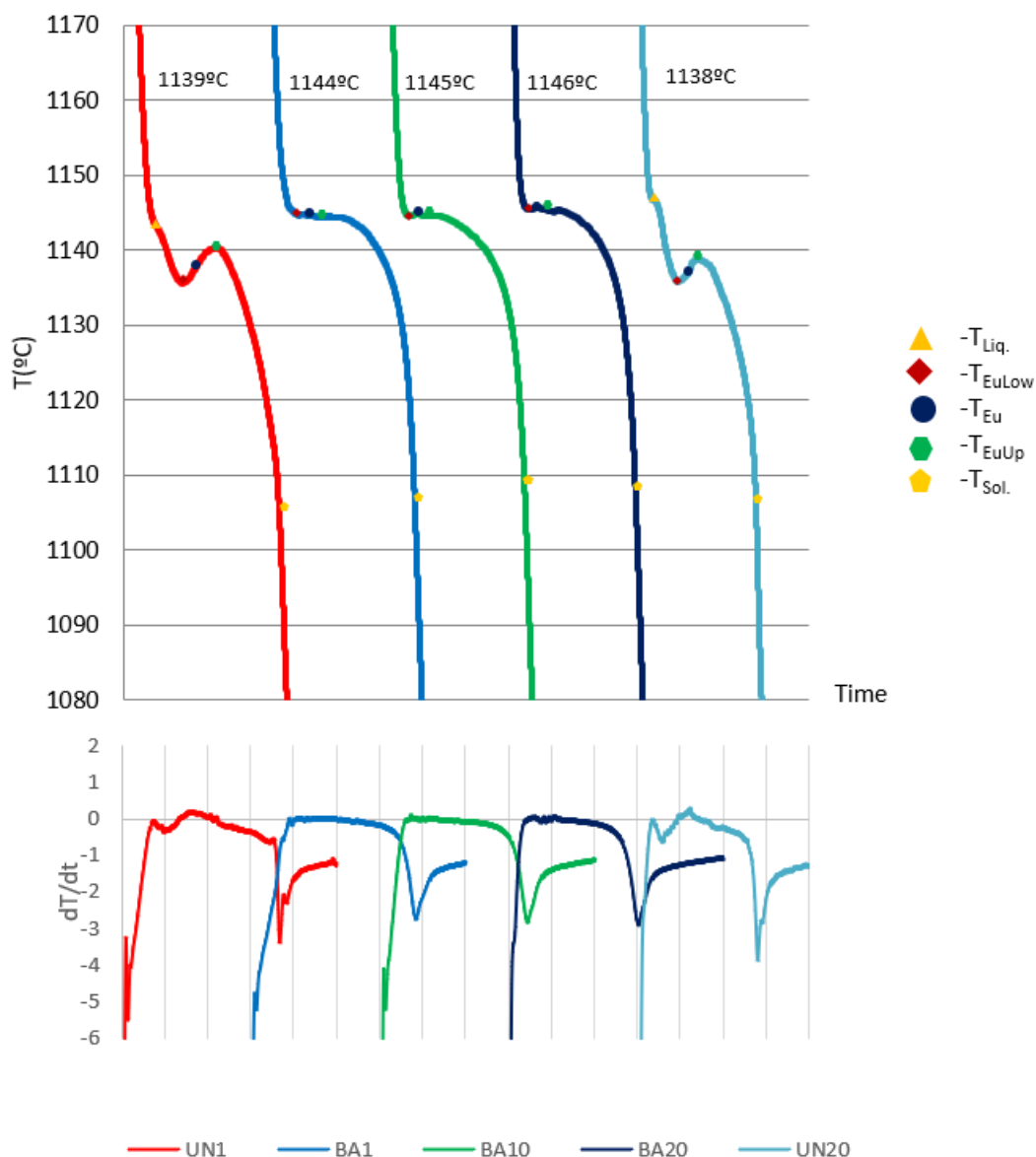
Figure 38. Solidification curves obtained during trials from the open cups' chambers Ba-FeSi inoculant.

Figure 37 and **Figure 38**, the hyper-eutectic curves obtained for the un-inoculated melts show two main plateaus. A primary one, without any recalescence, is considered to be the liquidus temperature and a second one, bigger than the first is considered to be the eutectic transformation.

The cooling curves of the un-inoculated open cup melts show an increase of distance from liquidus plateau to the eutectic plateau as time increases which means that there was a gain of carbon and silicon. This tendency was also observed in dual cups.

The cooling curves of the un-inoculated melts also show that the increase of holding time causes an increase of TEu$_{Low}$ however, the eutectic recalescence is much lower, which was also observed in the dual cups cooling curves.

Looking at the cooling curves of the Ca-inoculated melts in **Figure 32**, all the curves suggest an eutectic solidification morphology because they have only one plane plateau,

while the dual cups cooling curves are hyper-eutectic curves which are in accordance with the final chemical composition. Therefore, the solidification morphology of the open cups shows a discrepancy with the chemical composition.

Observing the cooling curve CA1 it is visible that the TEu_{Low} is slightly higher than the other curves and that the recalescence is very intense. Similar behaviour can also be observed in the cooling curve of sample CA1 in dual cups. As time increases, TEu_{Low} remains constant, but the recalescence is not so intense.

Figure 38 shows that all the Ba-inoculated samples also have a eutectic solidification morphology while the dual cups cooling curves are hyper-eutectic curves. Once again, the solidification morphology of the open cups shows a discrepancy with the chemical composition. Also, the eutectic curves obtained for the Ba-inoculant are similar.

Therefore, the use of open cups to anticipate the evolution of solidification demonstrates that it is not the best option compared to the dual cups since the cooling curves of the inoculated melts aren't in accordance with what the final chemical composition suggests. In addition, the effect of the fading of the (Ca, Al), FeSi inoculant isn't as visible in the cooling curves of the open cups as in the dual cups.

According to Stefanescu [26], the consistency of the data provided by the thermal analysis depends heavily on the pouring temperature and the cooling rate, which depends strongly on the mass of the metal in the cup. A higher pouring temperature and a greater mass affect significantly the undercooling and these factors are both difficult to control with the one-cup system as not only does the sensible heat vary but there is also a loss of the heat to the surroundings (the test cup and the atmosphere). Therefore the reliability of the interpretation and comparison of the thermal analysis cooling curves is low [26].

4.2.3. Comparison of the Morphology of the Cooling Curves of Dual Cups and Step Castings

Figure 39 and **Figure 40** show the solidification curves from thermal analysis step castings cups for the 5 mm and 20 mm sections, respectively.
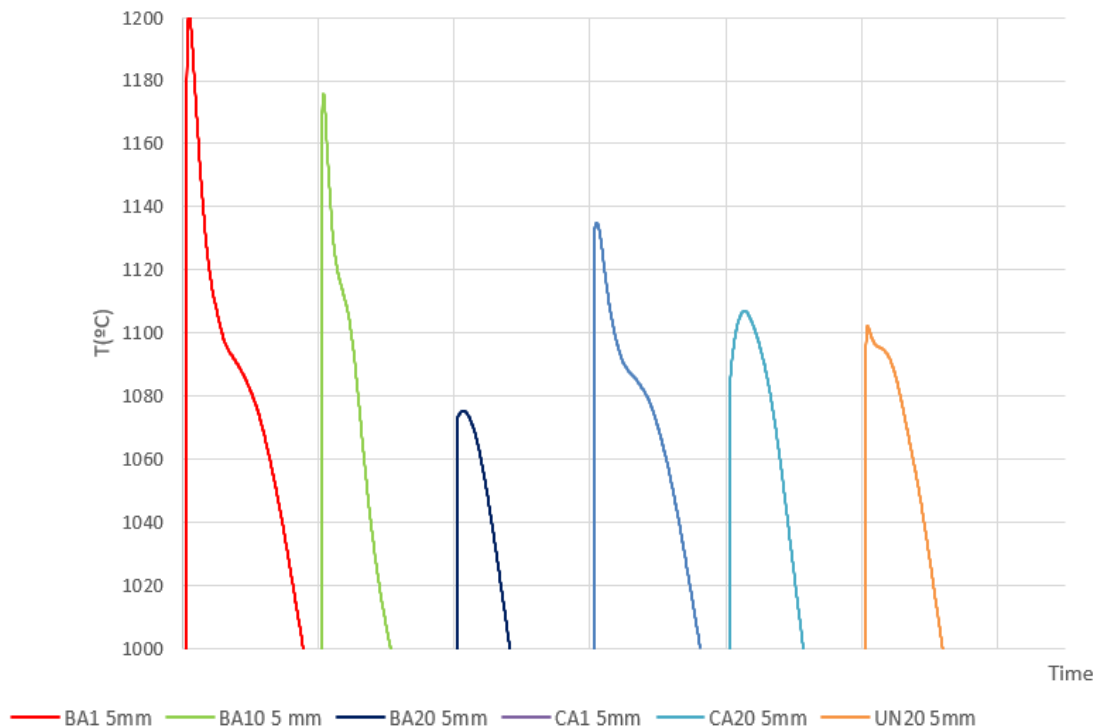
Figure 39. Solidification curves obtained during trials from 5 mm section of the step castings.
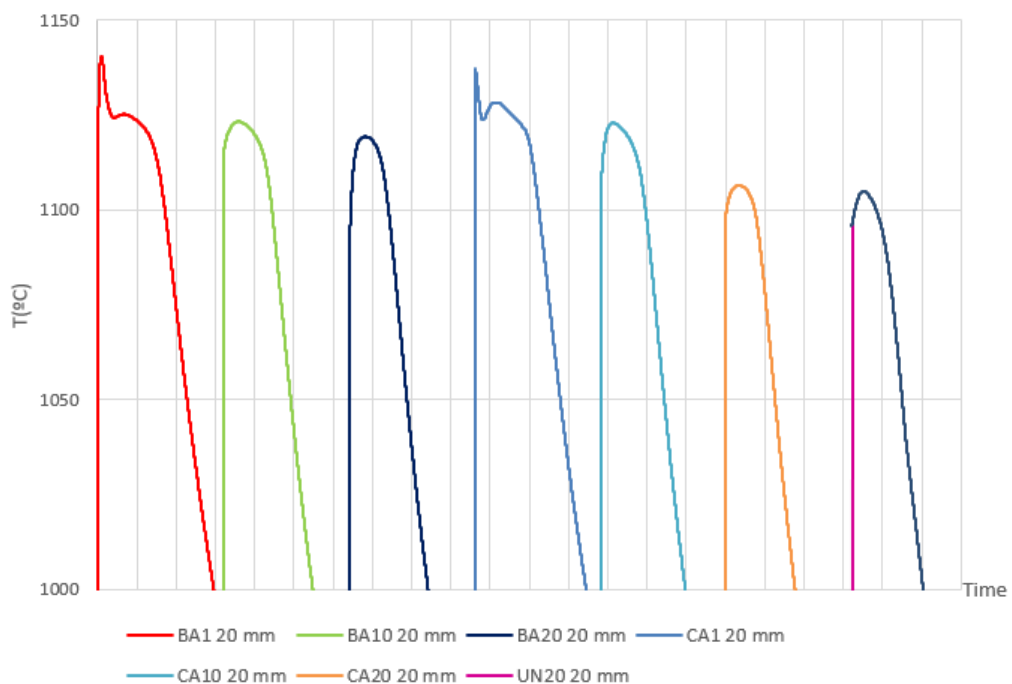
Figure 40. Solidification curves obtained during trials from 20 mm section of the step castings.

For this work, it was supposed to compare the cooling curves and microstructure of the step casting with the cooling curves of the dual cups. However, it was found that the temperatures of the majority of the cooling curves of the step casting were not recorded before the liquidus temperature (where there is no phase transformation), so it was not

possible to determine the cooling rate in the different sections of the mould cast and it was not possible to compare directly any of the cooling curves of the sections of the moulds cast with the microstructure of the dual cups.

5. CONCLUSIONS

The following main conclusions were made:

- The use of the thermal analysis, through the evaluation of the main critical points of the solidification curve, provides information about the efficiency and fading of the inoculants:
  - Fading can be seen when comparing the cooling curves of the Ca-inoculated melt with 1 minute of holding time (CA1) with the 10 minutes of holding time (CA10): is visible a decrease of TEu_{Low} and TEu_{Up} as well as time's extension of the eutectic plateau;
  - The cooling curves of Ba-inoculated melts have the same tendency as those inoculated with calcium: the plateau became shorter with holding time however, no decrease in TEu_{Low} and TEu_{Up} could be observed, which we presume that Ba-inoculant has a better fading's resistance than Ca-inoculant.
- In the dual closed cups, an increase of nodule count and nodularity was observed with the increase of holding time, for both inoculated melts, which was not excepted. The main reason may be due to the effect of decreasing pouring temperature, where cooler liquid of the 20 minutes holding time melts promoted nodule count.
- The dual closed cups suggest that fulfil their function of providing information on the efficiency of inoculation, because it is very clear the fading effect in the Ca-inoculated cooling curves and the fading resistance in the Ba-inoculated cooling curves.
- Finally, it may be concluded that the open cups is not the best option when you want to compare the inoculant's efficiency or when you want to anticipate, while solidification occurs, the type of microstructure of the melt, because pouring temperature and the volume of metal in the cup affects significantly the undercooling decreasing reliability the cooling curves.
- For the step castings, no correlation was possible to be made between the cooling curves of the step casting and the dual cups, since liquidus temperature of most of the cooling curves were not recorded and therefore no reliable results could be presented.

6. SUGGESTIONS FOR FUTURE WORK

From a personal and professional point of view, this work has enabled me to put into practice much of the knowledge acquired during my university education.

However, I believe that this work should be rethought and repeated. Therefore, the following are suggestions that can be made for future work:

- Repeat this work, changing the holding times to shorter ones, since in industry, companies don't practice such long holding times, which will decrease the pouring temperature effect factor and will allow a clearer evaluation, not only of the reliability of open and closed cartridges but also on the efficiency of Ca-FeSi and Ba-FeSi inoculants.
- Analysing the type of inclusions that make the heterogenous nucleation of graphite favourable.
- Use of the thermal analysis applied to the study of other inoculants with higher inoculation potential than Ca-FeSi and Ba-FeSi inoculants, such as (Ce)-containing inoculants.
- Evaluate the effect of most relevant addition active elements present in the different inoculants.
- Testing with step casting is useful but requires the use of more sensitive thermocouples, maybe using thinner K-Type only painted with refractory wash.

BIBLIOGRAPHIC REFERENCES

[1] Stefanescu, D.M; 2017; "Modification and Inoculation of Cast Iron" in ASM Handbook; Volume 1A - Cast Iron Science and Technology; ASM International.

[2] A. S. M. International Handbook Committee; 2017; "Carbon Equivalent", in ASM Handbook; Volume 15 – Casting; ASM International.

[3] Anjos, V.; 2015; "Use of Thermal Analysis to Control the Solidification Morphology of Nodular Cast Irons and Reduce Feeding Needs" in PhD Engineering Sciences; University of Duisburg-Essen.

[4] Stefanescu, D.M; 2017; "Matrix Microstructures of Ductile Irons" in ASM Handbook; Volume 1A - Cast Iron Science and Technology; ASM International.

[5] Colpaert, H.; 2018; "Nodular Cast Iron or Ductile Cast Iron" in Metallography of Steels - Interpretation of Structure and the Effects of Processing; ASM International.

[6] Mullins J.D.; 1990; "Ductile iron data for design engineers"; Rio Tinto Iron & Titanium Inc.

[7] Davis, J. R.; 1996; "Metallurgy and Properties of Ductile Irons", in ASM Specialty Handbook Cast Irons; ASM International.

[8] Forrest, R.D; 2006; "What Is The Optimum Base Sulphur Content Prior To Nodulatisation?" Cited 2020 15/04; Available from: http://www.sorelmetal.com/en/publi/PDF/095_(2006).pdf.

[9] American Foundry Society; 2006; "Carbon Equivalent - The C-SI Relationship" in Ductile Iron Handbook; American Foundry Society.

[10] Campbell, F.C; 2017; "Cast Irons", in Elements of Metallurgy and Engineering Alloys; ASM International.

[11] Leicon, F; 2020; "Iron-carbon phase diagram" Cited 2020 13/06; Available from: https://www.giessereilexikon.com/en/foundry-lexicon/Encyclopedia/show/iron-carbon-phase-diagram-4283/?cHash=a0427277d5037a18fa0c3db8c06c573f.

[12] METMAT; 2013; "Físico-Química para Metalurgia e Materiais I" Cited 2020 12/01; Available from: https://edisciplinas.usp.br/pluginfile.php/3371755/mod_resource/content/0/PMT3205_13.pdf.

[13] Zhou, J.; 2011; "Colour Metallography of Cast Iron" in China Foundry; Volume 6 No.2.

[14] Rudnev, V., Totten G.E.; 2014; "Other Processes of Magnesium Treatment" in ASM Handbook; Volume 04C - Induction Heating and Heat Treatment; ASM International.

[15] Rudnev, V., Totten G.E.; 2014; "Pouring Magnesium-Treated Melts" in in ASM Handbook; Volume 04C - Induction Heating and Heat Treatment; ASM International.

[16] Skaland, T., Ø. Grong, and T. Grong; 1993; "A Model For The Graphite Formation In Ductile"; Metallurgical Transactions ; Volume 24 (10): p.2321-2345.

[17] ASK Chemicals; 2020; "Inoculation of Cast Iron" Cited 2020 18/04; Available from: https://www.ask-chemicals.com/fileadmin/user_upload/Download_page/professional_articles/EN/Inoculation_of_cast_iron.pdf.

[18] Stefanescu, D.M.; "Liquid Treatment" in ASM Handbook; Volume 1A - Cast Iron Science and Technology; ASM International.

[19] Fredriksson, H., Åkerlind, U.; 2012; "Solidification and Crystallization Processing" in Metals and Alloys; Wiley.

[20] Stefanescu, D., Alonso, and Suarez; 2020; "Recent Developments in Understanding Nucleation and Crystallization of Spheroidal Graphite" in Iron-Carbon-Silicon Alloys; Metals; Volume 10.

[21] Bramfitt, B.L; 1970; "The effect of carbide and nitride additions on the heterogeneous nucleation behavior of liquid iron" Metallurgical Transactions; Volume 1

[22] Gruzleski, J.E; 2000; "Homogeneous Nucleation" in Microstructure Development during Metalcasting; American Foundry Society.

[23] Olander, D. R. and Motta, A.T.M; 2017; "Homogeneous Nucleation" in Light Water Reactor Materials; Volume 1 – Fundamentals; ANS (American Nuclear Society).

[24] A. S. M. International Handbook Committee; 1998; "Quantitative Thermal Analysis" in ASM Handbook; Volume 15 – Casting; ASM International.

[25] Heraeus Electro-Nite; 2020; "QuiK-Cup®, QuiK-Lab® E: Thermal Analysis of Cast Iron" Cited 2020 26/04; Available from: https://www.heraeus.com/media/media/hen/media_hen/products_hen/iron/QuikLabE_QuikCup_EN_lowres.pdf.

[26] Stefanescu, D., Suárez, and Kim S.; 2020; "90 years of thermal analysis as a control tool in the melting of cast iron" in China Foundry; Volume 17: p. 69-84.

[27] Thermocoupleinfo; 2011; "Type S Thermocouple"; Cited 2020 26/04; Available from: https://www.thermocoupleinfo.com/type-s-thermocouple.htm.

[28] Thermocoupleinfo; 2011; "Type K Thermocouple"; Cited 2020 26/04; Available from: https://www.thermocoupleinfo.com/type-k-thermocouple.htm.

[29] Measurement Computing Corporation; 2020; "DT8874 MEASURpoint"; Cited 2020 15/04; Available from: https://www.mccdaq.com/Products/MEASURpoint-Temperature-Instruments/DT8874-MEASURpoint.

[30] Abbott, S.; 2017; "Ostwald Ripening" in Surfactant Science - Principles & Practice; DEStech Publications.

ANNEXE A:

Table 5. Chemical composition of Cast Materials*

Unit		FB.01	FB.02	FB.10	BA1 A	BA1 B	CA1 A	CA1 B	BA10 A	BA10 B	CA10 A	CA10 B	BA20 A	BA20 B	CA20 A	CA20 B	UN1 A	UN1 B	UN20
%	C	3.85	3.87	3.77	3.73	3.65	3.73	3.65	3.78	3.66	3.66	3.71	3.64	3.74	3.62	3.7	3.69	3.76	3.76
%	Si	1.55	1.65	2.24	2.41	2.43	2.48	2.45	2.44	2.41	2.45	2.45	2.41	2.42	2.44	2.47	2.28	2.3	2.39
%	Mn	0.107	0.12	0.13	0.13	0.131	0.131	0.13	0.13	0.13	0.131	0.13	0.131	0.13	0.13	0.13	0.13	0.13	0.13
%	P	0.03	0.031	0.029	0.029	0.03	0.03	0.03	0.029	0.029	0.03	0.03	0.03	0.03	0.03	0.03	0.03	0.03	0.03
%	S	0.011	0.011	0.007	0.007	0.008	0.007	0.007	0.008	0.008	0.007	0.008	0.008	0.008	0.007	0.007	0.007	0.007	0.007
%	Mg	0	0	0.053	0.048	0.047	0.048	0.048	0.046	0.042	0.048	0.044	0.042	0.039	0.042	0.04	0.039	0.042	0.043
%	Ce	0.0031	0.0023	0.0049	0.0044	0.0049	0.005	0.0051	0.0046	0.0046	0.0049	0.0048	0.0046	0.0045	0.0045	0.0049	0.0046	0.0049	0.0048
%	La	0.0006	0.0005	0.0015	0.0013	0.0014	0.0015	0.0015	0.0014	0.0013	0.0015	0.0014	0.0014	0.0013	0.0013	0.0014	0.0013	0.0014	0.0014
%	Cu	0.0082	0.0085	0.01	0.0099	0.0103	0.0102	0.0106	0.01	0.0102	0.0101	0.0104	0.0104	0.0101	0.0101	0.0104	0.0102	0.01	0.011
%	Ni	0.0068	0.0073	0.007	0.0072	0.0076	0.0072	0.0073	0.0072	0.0071	0.0073	0.0075	0.0076	0.0074	0.0079	0.0075	0.0073	0.0072	0.0073
%	Cr	0.012	0.019	0.021	0.021	0.021	0.021	0.021	0.021	0.021	0.021	0.021	0.021	0.021	0.021	0.021	0.021	0.021	0.021
%	Al	0.0019	0.0019	0.0074	0.009	0.0091	0.0095	0.0095	0.0089	0.0086	0.0094	0.0088	0.0081	0.0076	0.0088	0.0084	0.0056	0.0073	0.0061
%	Ti	0.0085	0.0084	0.009	0.009	0.0092	0.0092	0.0092	0.0091	0.009	0.0092	0.0091	0.0092	0.0092	0.0092	0.0092	0.0089	0.0091	0.0091
%	V	0.0031	0.0031	0.0033	0.0032	0.0033	0.0034	0.0034	0.0033	0.0033	0.0033	0.0033	0.0033	0.0033	0.0033	0.0033	0.0033	0.0033	0.0033
%	Mo	<0.0007	<0.0007	<0.0007	<0.0007	<0.0007	<0.0007	<0.0007	<0.0007	<0.0007	<0.0007	<0.0007	<0.0007	<0.0007	<0.0007	<0.0007	<0.0007	<0.0007	<0.0007
%	Zr	<0.0004	<0.0004	<0.0004	<0.0004	0.0004	<0.0004	0.0004	<0.0004	0.0004	<0.0004	<0.0004	0.0004	<0.0004	<0.0004	0.0004	<0.0004	<0.0004	<0.0004
%	Sn	0.0013	0.0014	0.0019	0.002	0.0021	0.0021	0.0021	0.002	0.002	0.0022	0.0021	0.002	0.002	0.002	0.0021	0.0019	0.002	0.0021
%	Sb	0.0009	0.0009	0.0005	0.0006	0.0007	0.0006	0.0008	0.0006	0.0008	0.0007	0.0007	0.0007	0.0008	0.0007	0.0007	0.0009	0.0009	0.0008
%	Nb	0.0006	0.0006	0.0007	0.0007	0.0007	0.0007	0.0008	0.0007	0.0007	0.0007	0.0007	0.0007	0.0007	0.0007	0.0008	0.0007	0.0007	0.0007
%	CE	4.37	4.43	4.53	4.54	4.47	4.57	4.48	4.60	4.47	4.49	4.54	4.45	4.56	4.44	4.53	4.46	4.54	4.57

* Samples A were taken before being poured into the moulds, while Samples B were taken after the metal was poured into the moulds.

ANNEXE B:

Table 6. Main thermal analysis results from the solidification curves obtained during the trials of the dual cups.
TEuLow, TEuUp, TEut, Tliquidus and Tsolidus, respectively.

Dual Cups	TEuLow °C	TEuUp °C	TEut °C	Tliquidus °C	Tsolidus °C
Un-inoculated 1 min	1125	1127	1125	1135	1072
Un-inoculated 20 min	1126	1127	1130	1139	1072
Ba-FeSi 1 min	1135	1135	1135	1138	1072
Ca-FeSi 1 min	1139	1140	1140	1139	1077
Ba-FeSi 10 min	1138	1140	1138	1139	1075
Ca-FeSi 10 min	1137	1139	1135	1139	1076
Ba-FeSi 20 min	*	*	1137	1141	1080
Ca-FeSi 20 min	*	*	1136	1142	1072

* Unidentified values, since the first derivative of the respective samples did not have any zeros values

Table 7. Main results from microstructure parameter of the dual cups

Dual Cups	Nodularity (%)	σ	Nodule density (N/mm^2)	σ	Nodules size (μm)	σ
Un-inoculated 1 min	67	6	143	17	22	6
Ba-FeSi 1 min	77	5	236	15	21	4
Ca-FeSi 1 min	86	4	241	17	22	5
Ba-FeSi 10 min	87	5	298	22	21	4
Ca-FeSi 10 min	87	4	316	23	20	4
Ba-FeSi 20 min	89	4	328	14	20	4
Ca-FeSi 20 min	88	3	368	24	18	4

Table 8. Inclusion data from the dual cup's samples.

Casting	Holding Time (min)	da[μm]	σ	dv[μm] *	Nv (#/mm^2)
Un-inoculated	1	24	14	37.2	3010
Ba-FeSi	1	22	11	34.2	4219
Ca-FeSi	1	22	12	34.1	4308
Ba-FeSi	10	20	10	31.9	5328
Ca-FeSi	10	20	10	30.6	5740
Ba-FeSi	20	20	9	30.6	5805
Ca-FeSi	20	18	9	28.4	6346

d_A: arithmetic mean 2D inclusion diameter, d_V: arithmetic mean 3D inclusion diameter, Nv: number of particles

* Based on Fullman's theory for a monodispersed system of spheres, the measured 2D diameters were converted into 3D values through the following relation: $dv = \frac{\pi}{2} \cdot d_a$

Table 9. Main thermal analysis results from the solidification curves obtained during the trials of the open cups. TEuLow, TEuUp, TEut, Tliquidus and Tsolidus, respectively.

| Open Cups	TEuLow °C	TEuUp °C	TEut °C	Tliquidus °C	Tsolidus °C
Un-inoculated 1 min	1136	1141	1138	1143	1087
Un-inoculated 20 min	1136	1139	1137	1146	1094
Ba-FeSi 1 min	1144	1144	1144	1144	1095
Ca-FeSi 1 min	1145	1152	1149	1145	1106
Ba-FeSi 10 min	1145	1145	1145	1145	1098
Ca-FeSi 10 min	1144	1144	1144	1144	1091
Ba-FeSi 20 min	1145	1145	1145	1145	1094
Ca-FeSi 20 min	1145	1145	1145	1145	1097

ANNEXE C:
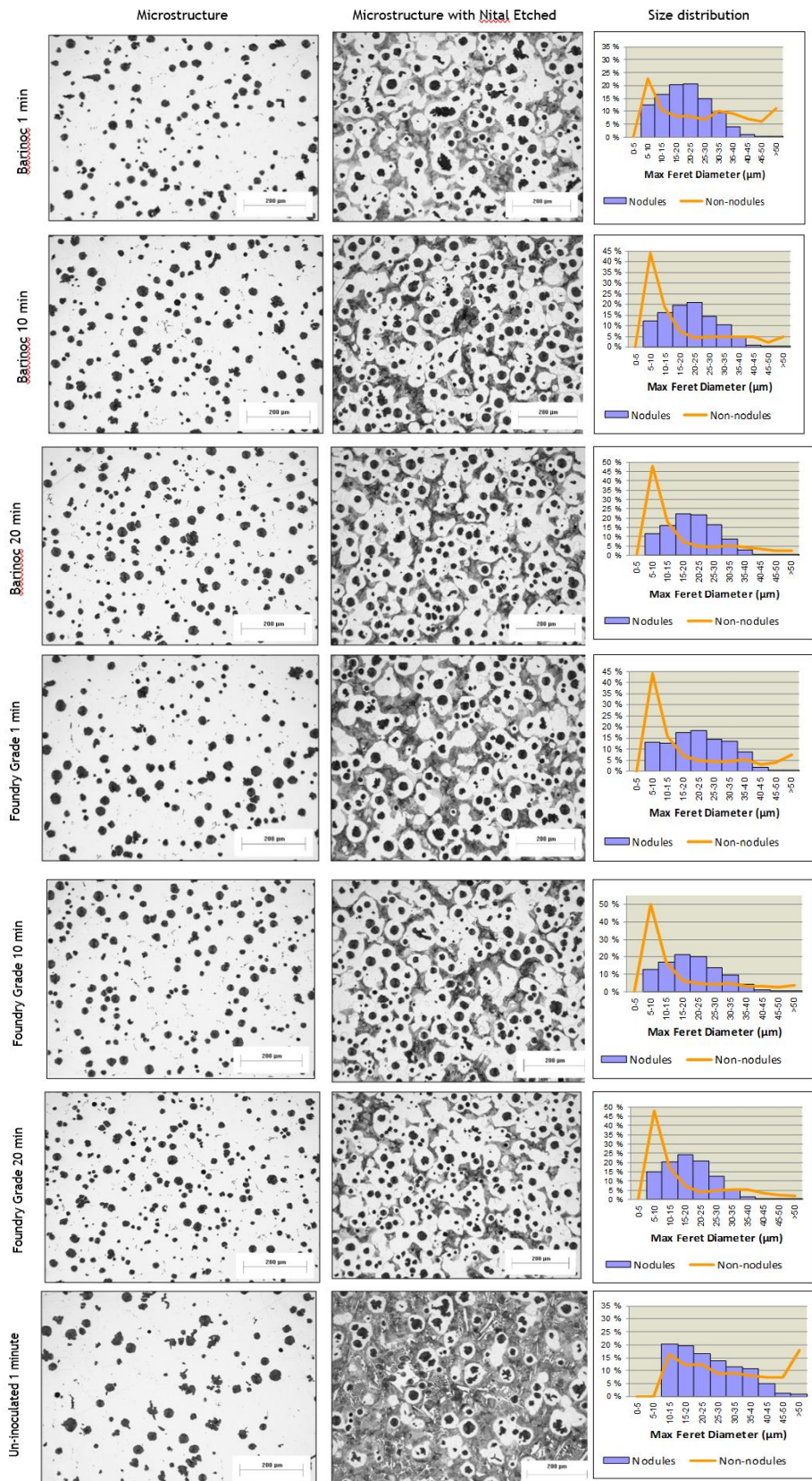
Figure 41. The microstructure of samples showing graphite nodules, ferrite/pearlite and size distributions of the dual cups.